Turun yliopisto
University of Turku

MAGNETOPHOTORESISTANCE IN $Pr_{1-x}Ca_xMnO_3$ THIN FILMS

Tomi Elovaara

TURUN YLIOPISTON JULKAISUJA – ANNALES UNIVERSITATIS TURKUENSIS
Sarja - ser. AI osa - tom. 542 | Astronomica - Chemica - Physica - Mathematica | Turku 2016

University of Turku

Faculty of Mathematics and Natural Sciences
Department of Physics and Astronomy
Wihuri Physical Laboratory

Supervised by

Prof. Petriina Paturi
Wihuri Physical Laboratory
Dept. of Physics and Astronomy
University of Turku
Turku, Finland

Dr. Hannu Huhtinen
Wihuri Physical Laboratory
Dept. of Physics and Astronomy
University of Turku
Turku, Finland

Dr. Sayani Majumdar
NanoSpin
Dept. of Applied Physics
Aalto Univesity School of Science
Espoo, Finland

Reviewed by

Asst. Prof. Ratnakar Palai
Department of Physics
University of Puerto Rico
San Juan, USA

Dr. Saumyadip Chaudhuri
Picodeon Ltd Oy
Piisilta 1
Ii, Finland

Opponent

Prof. Josep Fontcuberta
Institut de Ciència de Materials de Barcelona (ICMAB-CSIC)
Campus Universitat Autònomade Barcelona
Bellaterra, Catalonia, Spain

The originality of this thesis has been checked in accordance with the University of Turku quality assurance system using the Turnitin OriginalityCheck service.

ISBN 978-951-29-6507-6 (PRINT)
ISBN 978-951-29-6508-3 (PDF)
ISSN 0082-7002 (Print)
ISSN 2343-3175 (Online)
Painosalama Oy - Turku, Finland 2016

Preface

Acknowledgments

This work has been carried out in Wihuri Physical Laboratory of the Department of Physics and Astronomy at University of Turku. The Jenny and Antti Wihuri Foundation, the National Doctoral Programme in Materials Physics and the University of Turku Graduate School's Doctoral Programme in Physical and Chemical Sciences are acknowledged for financial support.

I wish to thank Asst. Prof. Ratnakar Palai and Dr. Saumyadip Chaudhuri for the insightful reviewing of this dissertation. I also want to thank Prof. Josep Fontcuberta, it is an honor to have you as my opponent. I would like to express my gratitude to Prof. Petriina Paturi whose effective supervision and efforts to arrange funding have made this thesis possible. I would also like to thank Dr. Hannu Huhtinen for countless hours spent with PLD and magnetometer, your help has been invaluable. Special thanks goes to Dr. Sayani Majumdar whose creative ideas have been an inspiration for this research. I also want to thank all the current and former colleagues in our research group, especially my brainstorming mate MSc Jussi Tikkanen for our deep conversations about PCMO, it has been a privilege to work with all of you.

I would like to thank my family for their love, caring and support and all of my friends for their relaxing company. Finally, I wish to thank my dearest Emmi for being there for me with your endless support and compassion. Words cannot ever describe how lucky I am to have you in my life.

Turku, June 2016

Tomi Elovaara

Abstract

In this work, a colossal magnetoresistive (CMR) $\mathrm{Pr}_{1-x}\mathrm{Ca}_x\mathrm{MnO}_3$ (PCMO) manganite thin films and polycrystalline samples were studied with the main focus on the properties of the insulator to metal Mott phase transition. The polycrystalline PCMO samples were fabricated with the solid state reaction method. The polycrystalline samples were further processed into the epitaxial thin films with the pulsed laser deposition method (PLD). The structural and magnetic properties of the samples were systematically investigated and the thin films samples were further investigated with magneto-transport measurement where the thin films response to illumination was also studied.

After the successful synthesis of polycrystalline PCMO samples with varying $x =$ between 0.0 - 0.5, the magnetic characterization of the samples showed rich magnetic properties having the signatures of the magnetic phase coexistence of antiferromagnetic (AFM) and ferromagnetic (FM) ordering and cluster glass behaviour. With the increased doping concentration from $x = 0.3$ to 0.5, the AFM charge-order (CO) phase started to form up being strongest on the sample $x = 0.5$. This AFM CO phase could be melted with the high external magnetic field at temperatures below Neel's temperature T_N inducing an irreversible first order metamagnetic AFM to FM phase transition. The strength of the AFM CO phase decreased with decreasing Ca concentration and increasing temperature.

The polycrystalline PCMO samples with Ca concentrations of 0.3 - 0.5, showing metamagnetic behaviour, were selected for the fabrication of the thin film samples. The films were grown using two different *in situ* oxygen treatment temperatures at 500 °C and 700 °C in the PLD system. The films with $x = 0.4$ and 0.5 showed weaker AFM CO phase with greatly reduced melting fields when compared to polycrystalline samples. Also, the robustness of the AFM CO phase was further decreased in thin films with the lower oxygen treatment temperature of 500 °C. The magneto-transport measurements made on the thin films showed that the melting of AFM CO phase was connected to CMR effect where the increasing magnetic field induced an insulator to metal phase transition, which reduces the resistivity of the film around nine orders of magnitude.

The use of illumination during the magneto-transport measurements showed a variety of intriguing phenomena including magnetophotoresistance. The illumination had a huge effect to the insulator to metal transition (IMT) reducing the transition magnetic field significantly. Moreover, by magnetically biasing the thin films with the constant external magnetic field, the IMT could be induced by switching on the illumination.

Tiivistelmä

Tässä työssä tutkittiin kolossaali magnetoresistiivistä (CMR) $\mathrm{Pr}_{1-x}\mathrm{Ca}_x\mathrm{MnO}_3$ (PCMO) manganitti materiaalia keskittyen Mottin eriste-metalli faasi transition ominaisuuksiin monikiteisissä kohtio sekä ohutkalvo näytteissä. Kohtiot valmistettiin kiinteän olomuodon menetelmällä, joista valmistettiin ohutkalvoja laserhöyrystysmenetelmällä. Näytteiden rakenteelliset ja magneettiset ominaisuudet tutkittiin. Lisäksi, valotuksen ja magneettikentän yhteisvaikutusta ohtukalvo näytteiden sähkönjohtavuusominaisuuksiin tutkittiin.

Valmistetun PCMO kohtiosarjan Ca-konsentratiota varioitiin välillä $x = 0.0$ - 0.5. Kohtio näytteiden magneettiset ominaisuudet sisälsivät viitteitä magneettisesta frustraatiosta sekä faasiseparaatiosta ferro- (FM) ja antiferromagneettisen (AFM) järjestäymisen välillä. Konsentraation $x = 0.3$ - 0.5 näytteillä havaittiin AFM varausjärjestynyt (CO) faasi, joka oli vahvin näytteessä $x = 0.5$. Tämä AFM CO faasi pystyttiin rikkomaan voimakkaalla magneettikentällä kriittisen lämpötilan T_N alapuolella, joka aiheutti irreversiibelin metamagneettisen ensimmäisen kertaluokan faasi transition AFM:sta FM:ksi. AFM CO faasi heikentyi nousevan lämpötilan funktiona sekä näytteen Ca konsentraation pienentyessä.

Metamagneettisen transition omaavista kohtioista, $x = 0.3$ - 0.5, valmistettiin ohutkalvo näytteet. Ohutkalvot kasvatettiin käyttäen kahta erilaista *in situ* happikäsittelyä lämpötiloissa 500 °C ja 700 °C. Ohutkalvoissa $x = 0.4$ ja 0.5 havaittiin huomattavasti heikompi AFM CO faasi, joka pystyttiin rikkomaan huomattavasti heikommalla magneettikentällä verrattuna kohtio näytteisiin. Lisäksi, ohutkalvon matalampi happikäsittely lämpötila 500 °C:ssa heikensi AFM CO faasia edelleen. Resistiivisyysmittauksissa huomattiin, että metamagneettinen faasi transitio liittyi CMR ilmiöön, missä kasvavan magneettikenttän aiheuttama faasitransitio muutti materiaalin eristävästä metalliseksi tiputtaen näytteen resistiivisyyttä n. yhdeksän decadia.

Ohutkalvojen valotus mittauksissa havaittiin monia mielenkiintoisia ilmiöitä kuten magnetofotoresistanssi. Valotuksella oli suuri vaikutus eriste-metalli faasitransitiossa tarvittavaan magneettikenttään, jossa valotus pienensi tarvittavaa magneettikenttää huomattavasti. Lisäksi, magneettisella biasoinilla ohutkalvo pystyttiin herkistämään valon vaikutukselle, jolloin eriste-metalli faasitransitiossa saatiin aikaiseksi pelkästään valottamalla näyte. Valon vaikutus kasvoi laskevan lämpötilan funktiona.

Articles included in this thesis

This thesis is based on the experimental work carried out at the Wihuri Physical Laboratory, Department of Physics and Astronomy, University of Turku during the years 2012 – 2015. The thesis consists of an introductory part and of the following publications:

[**P1**] T. Elovaara, H. Huhtinen, S. Majumdar and P. Paturi: *Irreversible metamagnetic transition and magnetic memory in small-bandwidth manganite* $Pr_{1-x}Ca_xMnO_3$ ($x = 0.0 – 0.5$), J. Phys.: Condens. Matter **24**, 216002 (2012).

[**P2**] T. Elovaara, H. Huhtinen, S. Majumdar and P. Paturi: *Linear and nonlinear ac susceptibilities* $Pr_{1-x}Ca_xMnO_3$ *in polycrystalline low-bandwidth* ($x = 0.0 – 0.3$) *manganite*, J. Phys.: Condens. Matter **26**, 266005 (2014).

[**P3**] T. Elovaara, H. Huhtinen, S. Majumdar and P. Paturi: *Study of dynamic magnetism in low bandwidth manganite* $Pr_{1-x}Ca_xMnO_3$ ($x = 0.3 – 0.5$) *by AC susceptibility measurements*, J. Low Temp. Phys. **175**, 554 (2014).

[**P4**] T. Elovaara, T. Ahlqvist, S. Majumdar, H. Huhtinen and P. Paturi: *Melting of the charge-ordered state under substantially lower mag- netic field in structurally improved* $Pr_{1-x}Ca_xMnO_3$ ($x = 0.3 – 0.5$) *thin films*, J. Magn. Magn. Mater. **381**, 194 (2015).

[**P5**] T. Elovaara, S. Majumdar, H. Huhtinen and P. Paturi: *Photoinduced colossal magnetoresistance under substantially reduced magnetic field*, Adv. Funct. Mater. **25**, 5030 (2015).

Articles relevant to this work but not included in this thesis

[**P6**] T. Elovaara, H. Huhtinen, S. Majumdar and P. Paturi: *Optimization of* $Pr_{0.9}Ca_{0.1}MnO_3$ *thin films with varying in-situ oxygen annealing treatments*, EPJ Web of Conferences **40**, 15011 (2013).

[**P7**] S. Majumdar, T. Elovaara, H. Huhtinen, S. Granroth and P. Paturi: *Crystal asymmetry and low-angle grain boundary governed persistent photoinduced magnetization in small bandwidth manganites*, J. Appl. Phys. **113**, 063906 (2013).

[**P8**] S. Majumdar, K. Kooser, T. Elovaara, H. Huhtinen, S. Granroth and P. Paturi: *Analysis of electronic structure and its effect on magnetic properties in (001) and (110) oriented* $La_{0.7}Sr_{0.3}MnO_3$ *thin films*, J. Phys.: Condens. Matter **25**, 376003 (2013).

[**P9**] S. Majumdar, H. Huhtinen, T. Elovaara and P. Paturi: *Stronger photo-induced effect in epitaxial thin films of small-bandwidth manganite* $Pr_{1-x}Ca_xMnO_3$ *compared to the polycrystalline bulk*, J. Supercond. Nov. Magn. **28**, 197 (2015).

[**P10**] M. Nyman, T. Elovaara, J. Tikkanen, S. Majumdar, H. Huhtinen ja P. Paturi: *Epitaxially textured* $Pr_{0.6}Ca_{0.4}MnO_3$ *thin films under considerably low substrate temperature.* Phys. Procedia **75** 1122 (2015).

[**P11**] T. Elovaara, S. Majumdar, H. Huhtinen and P. Paturi: *Defect induced enhanced low field magnetoresistance and photoresponse in* $Pr_{0.6}Ca_{0.4}MnO_3$ *thin films*, Phys. Procedia **75** 62 (2015).

[**P12**] T. Elovaara, S. Majumdar, H. Huhtinen and P. Paturi: *Photo-induced insulator-metal transition in* $Pr_{0.6}Ca_{0.4}MnO_3$ *thin films: effect of thickness dependent structural properties*, Appl. Srf. Sc. *accepted* (2016).

Contents

1 Introduction

1.1 Motivation

The success and the development speed of information technology have been outstanding and created very high demands for electronic components that it uses. However, in recent years, the processor clock speeds have not increased as the size of the single transistor is reaching of its physical limit. Hence, the devices that provide computational logic but are not transistor based, such as spintronics and memristors have been under increasing investigation. Alongside, the speed and storage space of memory devices continues to increase and hence the memory elements have become the main components to increase the performance of the computer. Particularly, the advances in the writing and reading speeds of mass storage memory devices have taken a leap with solid state drives. However, the data storage density of the memory devices is getting higher and higher towards the superparamagnetic limit.

All these considerations have challenged the industry to harness new materials with different functionality to achieve even faster, more compact and electrically efficient components. In particular, the transition metal oxides showing many interesting physical phenomena, ranging from high-T_c superconductivity in layered cuprates, colossal magnetoresistance (CMR) in perovskite manganites to multiferroicity, have been under intensive studies.

The correlated electron systems such as perovskite manganite compounds hold a very high promise for integration in micro- and nano-electronic components for potential applications in resistive memories, memristors and spintronics. Manganites show remarkable functionality with insulator to metal phase transition where the magnetic and transport properties of the material are influenced by external stimuli, such as electric or magnetic field, illumination or pressure. The external stimuli induce a nonvolatile insulator to metal resistive switching as the strongly correlated electrons of the initial Mott insulator state are released to the conduction band. These insulator to metal phase transitions are quite complex showing novel material physics with the interplay of charge, spin, orbital and crystal orderings, not yet completely understood and hence a topic of great scientific and technological interest. Also, an important aspect for applications is to study how to efficiently induce these phase transitions. That is why a fundamental physical understanding of these insulator to metal phase transitions is needed.

The $Pr_{1-x}Ca_xMnO_3$ (PCMO) manganite is a classic case of the material showing a huge CMR effect which makes PCMO an excellent material to study the physics of the insulator to metal phase transition in manganites. Although, the PCMO is not an ideal candidate for applications, it is a prototypical system for studying and understanding complex phase correlation that can be used in practical devices. Usually, the insulator to metal transition (IMT) in manganites is studied only under the single external stimulant. However, in this thesis, the more efficient IMT transition is studied under the joint effect of multiple external stimulants. The first part of this thesis discusses the basic physical concepts of the manganites, PCMO and the used experimental methods together with sample preparation. Thereafter, the second part covers the structural and magnetic properties of polycrystalline PCMO with varying Ca concentration x between 0.0 - 0.5. In the third part of the thesis, the IMT properties are studied under the magnetic field in differently *in situ* annealed thin film samples with x varying between 0.3 - 0.5. The final part of the thesis includes the dynamical magnetophotoresistance measurements of the films where the IMT is studied under the combined stimulants of illumination and magnetic field.

1.2 Manganites

The Manganese (Mn) based perovskite oxides, which are often called manganites, have the general chemical formula of $\mathrm{ABO_3}$, where the A site is occupied by trivalent rare earth metal (RE) or divalent alkaline earth metal (AE) and the B site with Mn transition metal. The ideal simple cubic perovskite structure is presented in figure 1, where the A sites are located at the corners of the cubic structure and the B site is in the middle of the cube surrounded by oxygen octahedron. The stability and distortion of the perovskite crystal structure can be described By the Goldschmidt tolerance factor [1]

$$t = \frac{r_\mathrm{A} + r_\mathrm{O}}{\sqrt{2}(r_\mathrm{B} + r_\mathrm{O})}, \tag{1}$$

where r_i ($i =$ A, B and O) is the corresponding ionic radii of elements in the perovskite structure (A = RE, AE and B = Mn) [9]. When the t lies between 0.9 - 1, the perovskite structure has the ideal cubic symmetry. However, the structure starts to get more distorted with smaller t between 0.7 - 0.9 producing orthorhombic or rhombohedral lattice symmetry [2]. Hence, by reducing the size of the A site atom, the perovskite structure of the manganite material gets more distorted, as the oxygen octahedra get tilted and the Mn-O-Mn bond angles bend away from 180°.

By partially replacing (doping) the rare earth metal in the manganite compound with different size alkaline earth metal ($\mathrm{RE_{1-x}AE_xMnO_3}$), we can adjust the t factor as well as the carrier concentration of the material. When the trivalent rare earth metals are

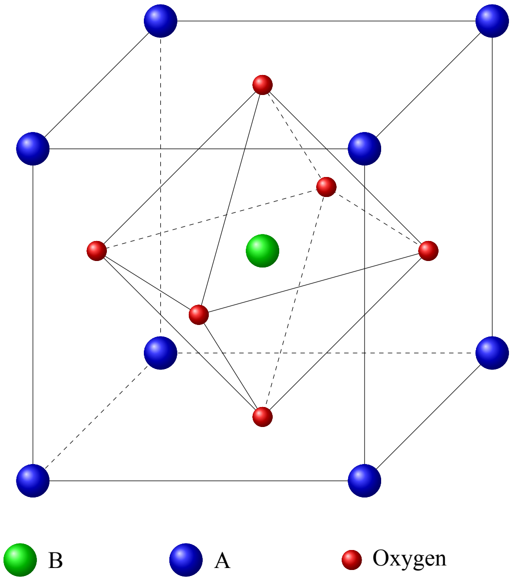

Figure 1. The ideal cubic perovskite structure.

replaced with divalent alkaline earth metals, the oxidation state of the manganese ions change from Mn^{3+} to Mn^{4+}. Hence, by changing the doping concentration, we can change the $\mathrm{Mn}^{3+}/\mathrm{Mn}^{4+}$ ratio of the manganite.

The partially filled $3d^{(3/4)}$ electron shell determines the magnetic and transport properties of the Mn ions. However, the measured magnetic moment of Mn ions does not follow the localized electron model for free ions. The d subshell electrons have large radial distance from the ion core compared to other subshells [3]. Hence, the $3d$ electrons in manganites sense the crystal field induced Coulomb interaction of the surrounding charge distribution of ligand oxygen ions [4]. This crystal field interaction quenches the orbital angular momentum (L) of d band electrons leaving only the spin angular momentum (S) to take apart to the magnetic moment of Mn ion [3, 4].

The crystal field that surrounds the Mn ions splits the five-fold degenerate energy orbitals of the d band into the lower triply degenerate $t_{2\mathrm{g}}$ and higher doubly degenerate e_{g} orbitals, as shown in figure 2. This kind of system, where the repulsion interaction between the electrons has to be taken into account to explain the magnetic and transport properties, is called the correlated electron system [5]. The Jahn-Teller (JT) effect further lifts the degeneracy of the $t_{2\mathrm{g}}$ and e_{g} energy levels for the Mn^{3+} ions inducing elongation distortion into the $\mathrm{Mn}^{3+}\mathrm{O}_6$ octahedra [4, 6], as displayed in the figure 2. The JT effect happens spontaneously as the system strives for energy minimum by

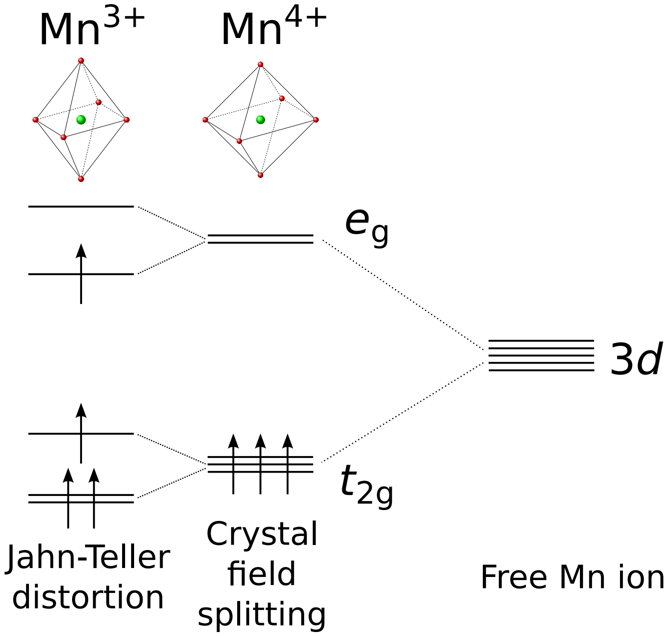

Figure 2. The crystal field splitting of the Mn $3d$ electron shell and Jahn-Teller distortion of Mn^{3+} ions.

decreasing the occupied e_g orbital energy. However, the Mn^{4+} are not affected by the JT distortion, as the t_{2g} subshell is half full and therefore the energy level splitting does not lower the overall energy of the subshells.

In conclusion, the hole doping of the rare earth manganites with alkaline earth metal changes the perovskite lattice distortion by affecting the t factor and the JT effect. Both of these distortions drive the Mn-O-Mn bond away from 180° and change the bond lengths, which have direct impact on materials prevailing magnetic and transport properties that will be discussed in the following section.

1.3 Magnetic interactions and transport mechanisms

1.3.1 Superexchange interaction

The magnetic properties of the manganites cannot be explained by the direct Heisenberg exchange interactions between Mn ions, because the ions are separated by nonmagnetic oxygen ions and the Mn ions are too far away from each other. Hence, the indirect magnetic exchange mechanism, called superexchange, plays a decisive role in determining the magnetic long range order in manganites.

In the superexchange interaction, the spins of the Mn ions interact with each other indirectly through the intermediary oxygen ion, forming a semicovalent bond [7, 8]. In the semicovalent bond, the energetically similar Mn e_g and O^{2-} $2p$ orbitals overlap, sharing the orbitals electrons, by means of virtual electron transfer, reducing the Mn - O bond length. The sign and strength of the superexchange interaction between the Mn ions are strongly dependent on the relative orientation, symmetry and electron population of the overlapping orbitals [9]. Luckily, the Goodenough-Kanamori-Anderson rules clarify the properties of the prevailing superexchange interaction for different situations as shown in figure 3 for $Mn^{3+/4+}$ - O bonds [9, 10].

The two valence electrons of the oxygen $2p$ orbital have the opposite spins due to Pauli exclusion principle. For the same reason, the hybridizing p and half filled Mn^{3+} e_g orbital electrons have the opposite spins as they are sharing the same orbital. Furthermore, the spin of e_g electron is aligned ferromagnetically with the local $t_{2\mathrm{g}}$ spins due the strong intra-site Hund's coupling. Thus, a relatively strong AFM interaction appears between the Mn^{3+} ions, as depicted in figure 3(a). Similarly, the hybridized empty e_g orbital of Mn^{4+} and the oxygen p orbital share one electron that is ferromagnetically coupled with the local $t_{2\mathrm{g}}$ spins due to Hund's rules (figure 3(b)), inducing relatively strong AFM interaction between Mn^{4+} ions. The rather weak FM interaction is also possible between Mn^{3+} and Mn^{4+} ions with 180 ° bond angle, as shown in figure 3(c).

As the tolerance factor and JT distortion affect the Mn - O - Mn bond length and angle, they also effectively change the overlapping of the orbitals and, hence, the properties of the superexchange interaction.

1.3.2 Double exchange interaction

The superexchange interaction cannot explain the metallic transport properties of some manganite materials as the superexchange interaction induces only insulating transport properties with the localized electrons. Hence, another magnetic interaction mechanism with itinerant electrons, called double exchange (DE) interaction, has been presented. The DE interaction is an indirect interaction between Mn^{3+} and Mn^{4+} ions where the conducting e_g electrons induce the FM coupling. The mobile electrons hop between Mn^{3+} and Mn^{4+} ions over intermediary oxygen ion as shown in figure 4(a) [11]. In the DE interaction, the electron hops from the oxygen $2p$ orbital to the empty e_g orbital of Mn^{4+} ion. Simultaneously, another electron hops from the Mn^{3+} e_g orbital to the oxygen $2p$ orbital. The transfer of the conducting electron between Mn^{3+}, Mn^{4+} and O^{2-} ions is energetically more favourable if the system does not have to flip the spin.

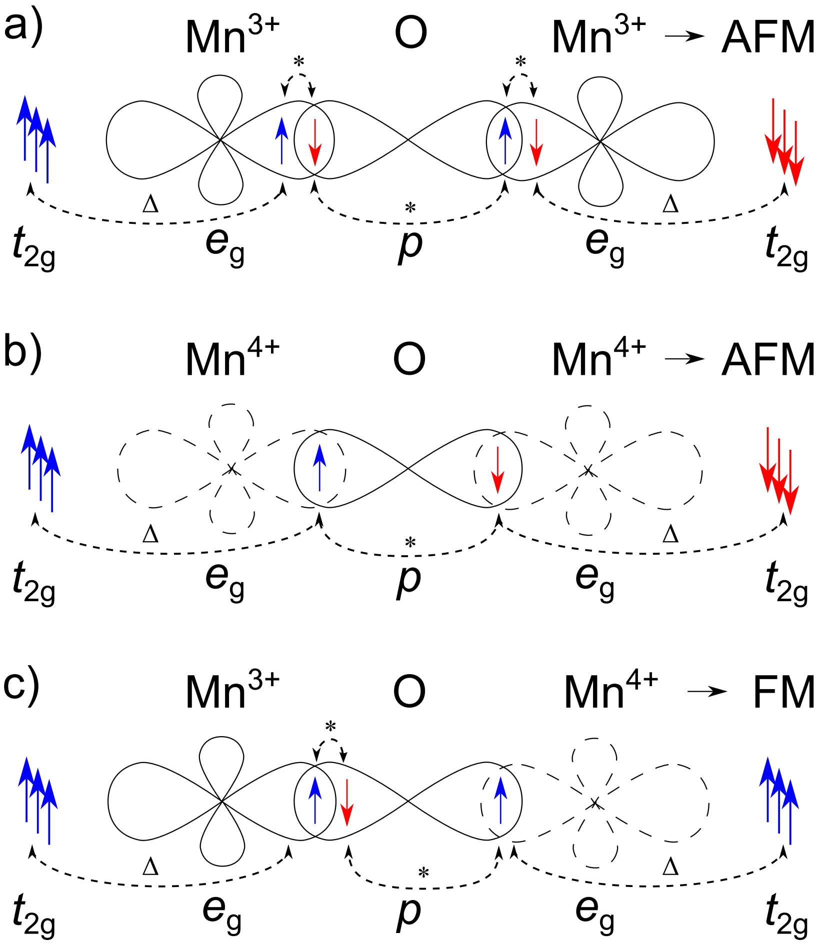

Figure 3. The Goodenough-Kanamori-Anderson rules give AFM superexchange interaction between (a) Mn^{3+} - Mn^{3+} and (b) Mn^{4+} - Mn^{4+} ions with 180° bond angle while the interaction between (c) Mn^{3+} - Mn^{4+} is FM. The symbols $*$ and Δ denote Pauli's exclusion principle and Hund's coupling, respectively.

This saves kinetic energy and makes the FM ordering preferable.

The DE interaction is also sensitive to the Mn - O - Mn bond angle, and as the electron's effective transition between adjacent Mn ions in the DE interaction follows the equation [5, 12]

$$t_{ij} = t^0 \cos(\theta_{ij}/2). \tag{2}$$

The electrons' effective hopping interaction t_{ij} depends on the relative angle θ_{ij} between the neighbouring i and j Mn ion $t_{2\mathrm{g}}$ spins, which is affected by tolerance factor and JT distortion. The t^0 is the normal transfer integral when all the spins are aligned. The schematic illustration of the situation is presented in figure 4(b). The electron transfer probability decreases and the interaction is weakened when the ferromagnetically coupled Mn - O - Mn bond is bent, decreasing the one electron bandwidth W and conductivity of the material.

The DE interaction is always ferromagnetic and it involves actual electron transfer, unlike the superexchange interaction where a static interaction is established without any charge transport. However, the DE interaction only gives an intuitive explanation for the insulator to metal phase transitions in the manganites but it fits poorly to the quantitative analysis of these materials [13]. Hence, more complicated systems have been suggested to explain these phenomena [14].

1.4 Colossal magnetoresistance

According to the band theory, the manganites with the partially filled d band are expected to be metallic [15]. However, this is not the case for the majority of manganites having an insulating phase at room temperature, as the electron correlations have to be taken into account when considering the transport properties of manganites. This is characteristic for materials called Mott insulators. The intrinsic property of Mott insulators is that the transport properties of the material can be influenced by changing the electric and magnetic field, temperature, hole concentration and the prevailing pressure, which leads to the insulator to metal phase transition *i.e.* Mott transition [16].

The distance between the magnetic ions in the Mott insulator structure has a direct impact on the material's electron bandwidth W. The closer the ions are to each other, the wider is the bandwidth. Hence, in the conventional Mott transition, the IMT is achieved by reducing the distance between ions, either decreasing temperature or increasing pressure. In the manganites, an increase of ionic radius of RE and AE atoms ($\mathrm{Pr}^{2+} < \mathrm{Ca}^{3+} < \mathrm{La}^{3+} < \mathrm{Sr}^{2+}$ [17]) increases the W as there is less space between atoms in the structure and, on the other hand, the crystal lattice becomes less distorted. Hence, for example,

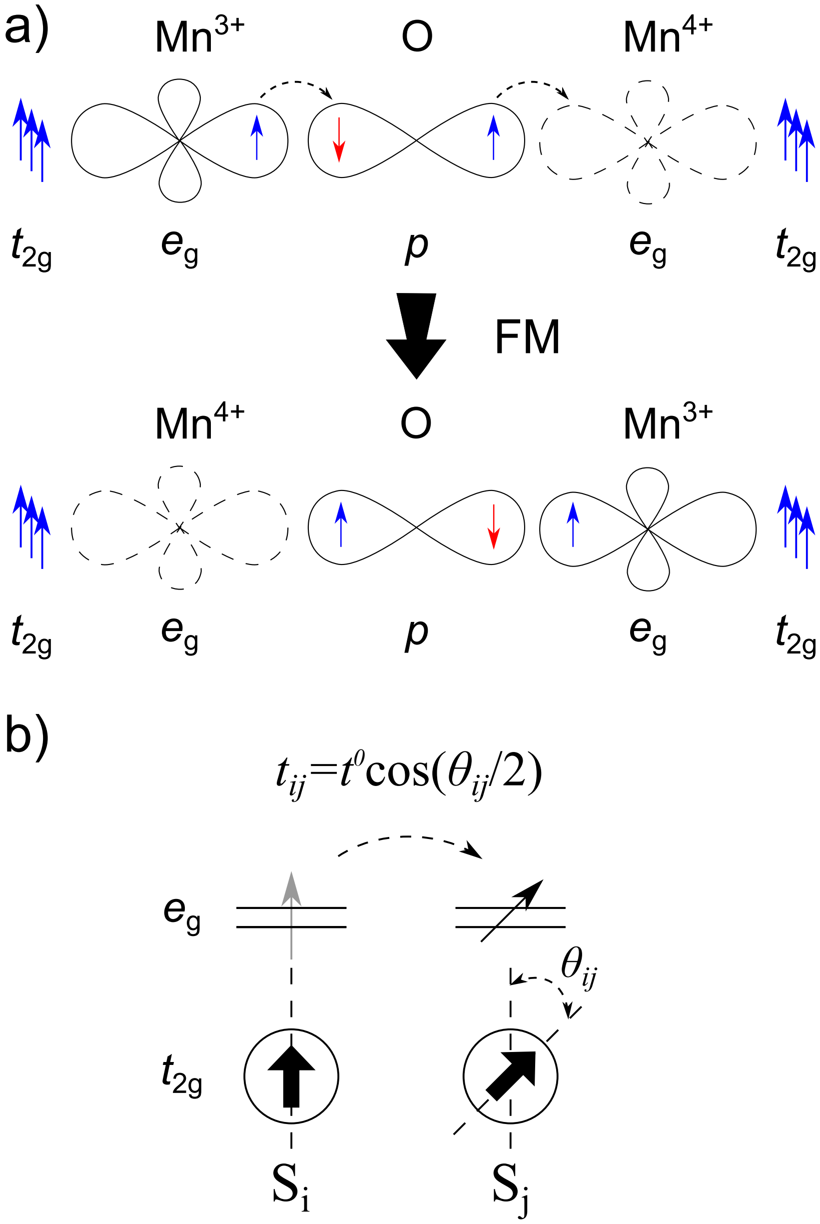

Figure 4. (a) A schematic representation of the DE mechanism, where the electron transfers from a Mn^{3+} ion to oxygen $2p$ orbital, while the $2p$ electron simultaneously hops to Mn^{4+} ion resulting charge transfer between Mn ions and FM interaction. (b) Illustration of the effective e_g electron transfer between Mn ions.

the $La_{1-x}Sr_xMnO_3$ manganite transforms from insulating to metallic phase when the Sr doping range exceeds the threshold value of $x \approx 0.2$ at 300 K [18].

In manganites, the external magnetic field induces the IMT where the resistivity of the material decreases several orders of magnitude and, hence, it is called a colossal magnetoresistance (CMR). Compared to the normal magnetoresistance $(\Delta R/R_{H=0})$, where the resistance increases 2% - 3% under the magnetic field [19], the effect of CMR is negative and exceptionally strong. However, the magnetic field does not directly reduce the distance between magnetic ions and therefore the mechanism of the CMR phenomenon differs from the conventional Mott transition. For the narrower W manganites, the initial phase becomes more insulating and the CMR effect more prominent.

1.4.1 Electron phonon coupling

The lattice around the conducting electrons in e_g band is distorted due the JT effect. These electrons conduct via hopping and carry the lattice distortion, *i.e.* phonon, from site to site with them. This kind of electron phonon coupling is called a JT polaron in manganites. As the tolerance factor decreases with doping, the JT splitting of the e_g band increases and the polarons get trapped due to the increased JT distortion, thereby decreasing conductivity.

The effective electron phonon coupling can be expressed [20]

$$\lambda_\mathrm{eff} = E_{JT}/t_\mathrm{eff}, \tag{3}$$

where the trapping energy (E_{JT}) describes the amount of JT distortion (e_g band splitting) and t_eff is the hopping amplitude. The larger the λ_eff coupling, the stronger is the polaron trapping which localizes the electrons. Hence, the transport properties of the material can be affected by external stimulants that either reduce the E_{JT} by decreasing the band gap between $t_{2\mathrm{g}}$ and e_g bands or increase t_eff via aligning the Mn ion spins.

1.4.2 Charge and orbital ordering

The strong JT coupling in the small or medium electron bandwidth manganites induces the localization of the conducting electrons, showing charge and orbital ordering (CO/OO) with the hole doping concentration around 0.5. In the CO state, the charge distribution forms a chequerboard pattern as presented in figure 5. Due to the strong electron lattice coupling, the CO phase transition is of the first order as it is accompanied with a structural phase transition [21–23]. The Mn^{3+} and Mn^{4+} ions form a

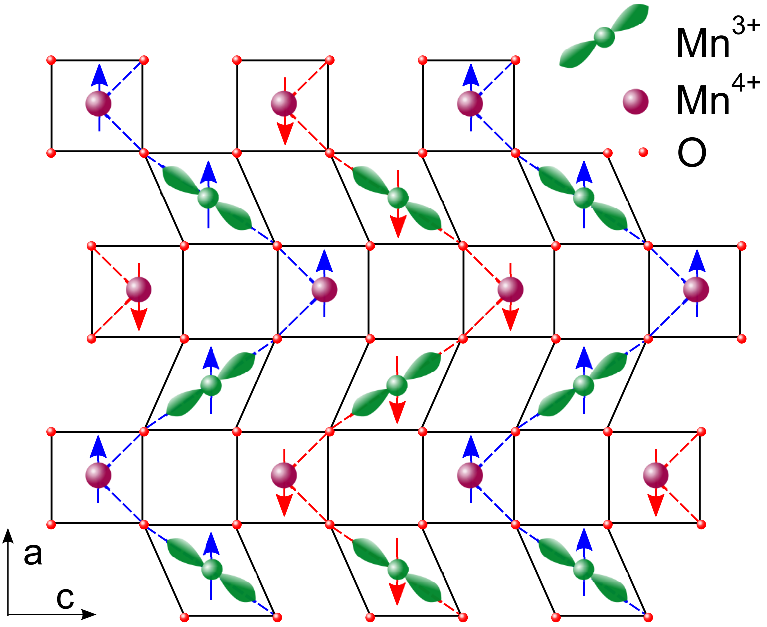

Figure 5. Schematic of AFM charge and orbital order of the Mn sites in the Mn–O plane.

chequerboard like arrangement where the Mn^{3+} ions have the orbital degree of freedom. The Mn spins form ferromagnetic zigzag chains, coupled antiferromagnetically to each other on the Mn-O plane [24]. The oxygen octahedra around Mn^{3+} ions get elongated along the chain direction due to the JT effect [25].

1.4.3 Nanoscale phase separation

The key component of the current theories, aiming to explain the CMR phenomenon in manganites, is the competition between the co-existing insulating AFM CO and metallic FM phases [26, 27]. The magnetic phase separation and phase co-existence are possible because the magnetic field induced phase transition from CO phase to FM phase is of the first order. During the first order phase transition process, the temperature of the system will stay constant as the heat is added into it and the system is in the co-existing phase regime in which some parts of the system have completed the transition and others have not. The random impurities broaden the first order phase transition so that the transformation occurs over a wider temperature or magnetic field range [28]. In the disorder-broadened CMR transition, the fraction of FM metallic phase grows

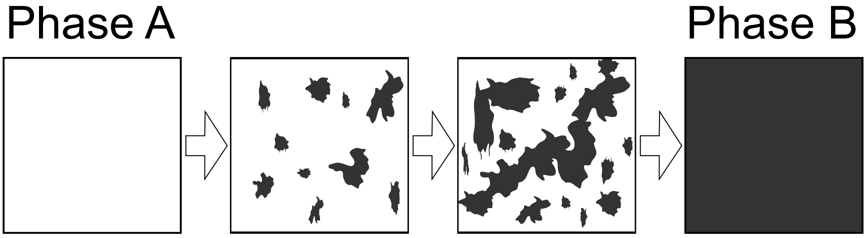

Figure 6. Discountinuous first order phase transition inducing nanoscale phase separation.

from zero to 100%, if the transition is completed, as shown in figure 6. Similarly, the first order magnetic phase transition can occur as a function of temperature, leading to a phase separation and co-existence of micro and nano sized clusters with different magnetic phase. The first order phase transition induces nanoscale phase separation or phase coexistence if the phase transition is not fully completed.

1.5 $Pr_{1-x}Ca_xMnO_3$

The Pr and Ca ions have a relatively small radius (inducing small t) which induces a quite large lattice distortion to the PCMO manganite. Hence, PCMO has a small electron bandwidth and it stays insulating for the whole doping regime. Because of the small ionic radii of Pr and Ca, the PCMO has orthorombic *Pnma* crystal system with tilted MnO_6 octahedra and bent Mn - O - Mn bonds as depicted for $x = 0.4$ in figure 7. The distorted lattice increases the JT coupling and the PCMO shows a very rich magnetic phase diagram including AFM and FM ordering together with stable CO phase as shown in figure 8. The magnetic field has a drastic effect on the properties of PCMO showing obviously larger CMR effect than found in other compounds [27].

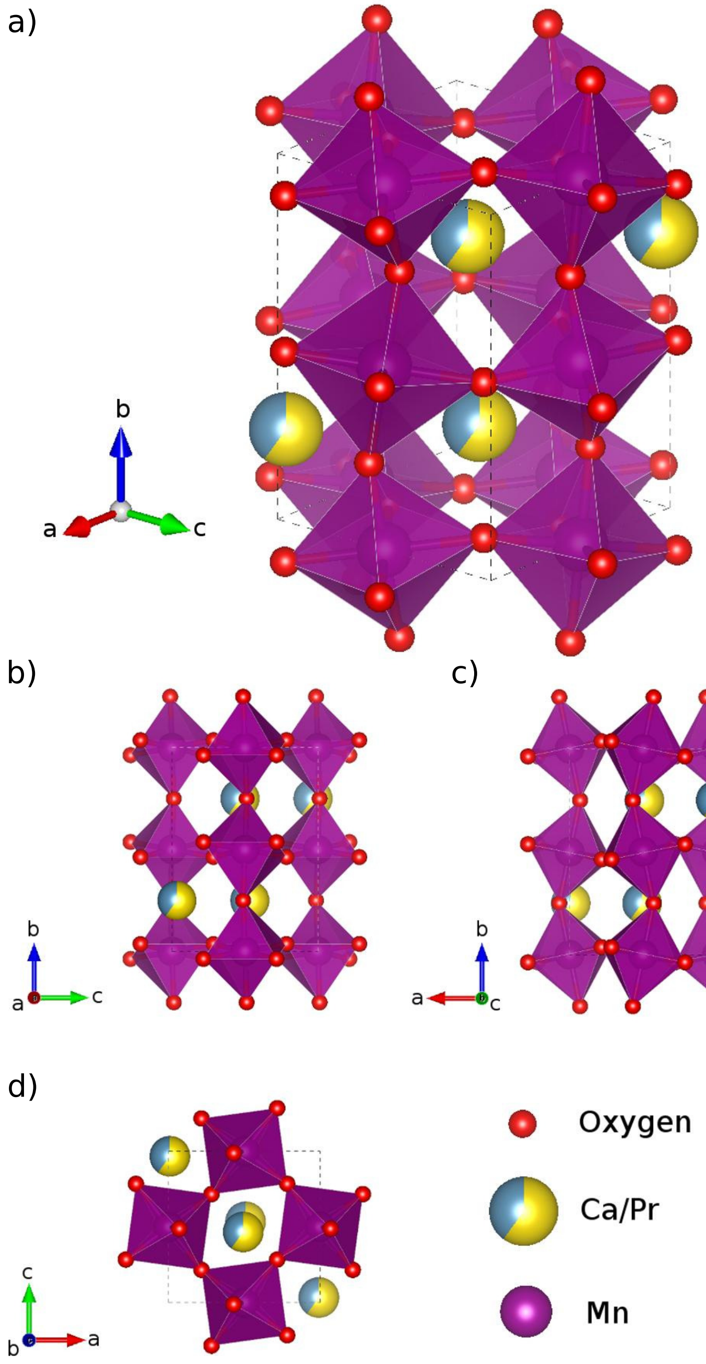

Figure 7. Orthorombic crystal structure of PCMO $x = 0.4$ unit cell from different viewing angles.

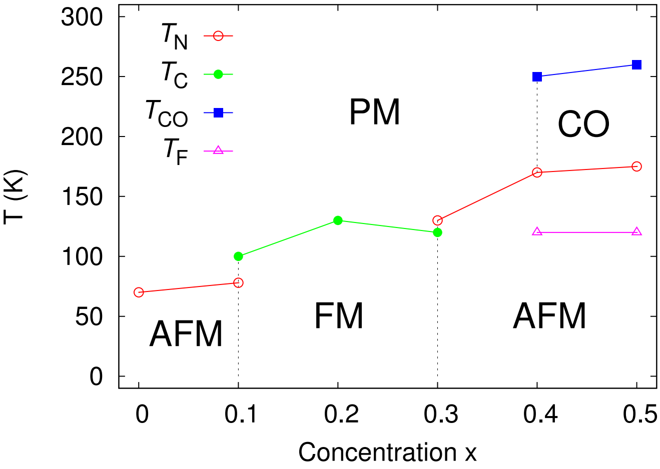

Figure 8. Magnetic phase diagram of PCMO $x = 0.0$ - 0.5 [**P1**, **P2**, **P3**]. The T_{N}, T_{C} and T_{CO} denotes Néel, Curie and CO transition temperatures, respectively. The T_{F} denotes the frustrated magnetic transition where it is not possible to arrange the FM and AFM couplings so that all the magnetic interactions are simultaneously satisfied [**P3**].

2 Experimental details

2.1 Sample preparation

2.1.1 Solid state reaction

Polycrystalline $Pr_{1-x}Ca_xMnO_3$ targets with concentrations of $x =$ 0, 0.1, 0.2, 0.3, 0.4 and 0.5 were prepared by the solid state reaction method, where the target material is synthesized from the powdered source materials through the diffusion reaction without any solvents [29]. First the weighted and dried high purity Pr_6O_{11}, $CaCO_3$ and Mn_2O_3 salts were mixed together. The stoichiometric balance between the source materials was calculated according to the chemical reaction $CaCO_3$ + Pr_6O_{11} + Mn_2O_3 $\rightarrow$ Pr_{1-x} Ca_x MnO_3 + CO_2 + O_2. The mixed powders were carefully ground for 30 min and then pressed into target pellets at 300 atm pressure. After this, the pressed targets were sintered at 1200 °C for 14 h in air. In order to produce a single-phase material the three-stepped process with grinding–pressing–sintering was repeated three times in total using 14, 36 and 36 h sintering sequences [**P1**].

2.1.2 Pulsed laser deposition

The PCMO films were fabricated using pulsed laser deposition (PLD) technique where the goal is to crystallize the target material on top of the substrate while maintaining the target stoichiometry [30]. In our PLD method, a target is ablated using high power nanosecond laser pulses from ultraviolet laser ($\lambda =$ 308 nm). When laser interacts with the target surface a plasma plume is created. The plume is adjusted so that the tip of the plume hits to the heated substrate where the thin film is deposited. A schematic description of the experimental setup is shown in figure 9.

During the deposition process, the background gas flow is adjustable which makes the PLD method particularly suited for depositing the complex oxide materials which are sensitive to the oxygen flow during deposition. Another way to control the oxygen content of the complex oxide thin films is to adjust the substrate temperature during the ablation process or afterwards during the *in situ* post-annealing process.

Another important requirement, in order to obtain well crystallized thin films from PLD technique, is that the used substrate material has similar lattice parameters as the target material. In our case, the PCMO thin films with in-plane lattice parameters around $a, c =$ 5.4 Å were deposited on top of the (100) $SrTiO_3$ (STO) substrate where a cubic crystal structure (lattice parameter of $a =$ 3.905 Å). Hence, the a, c lattice directions

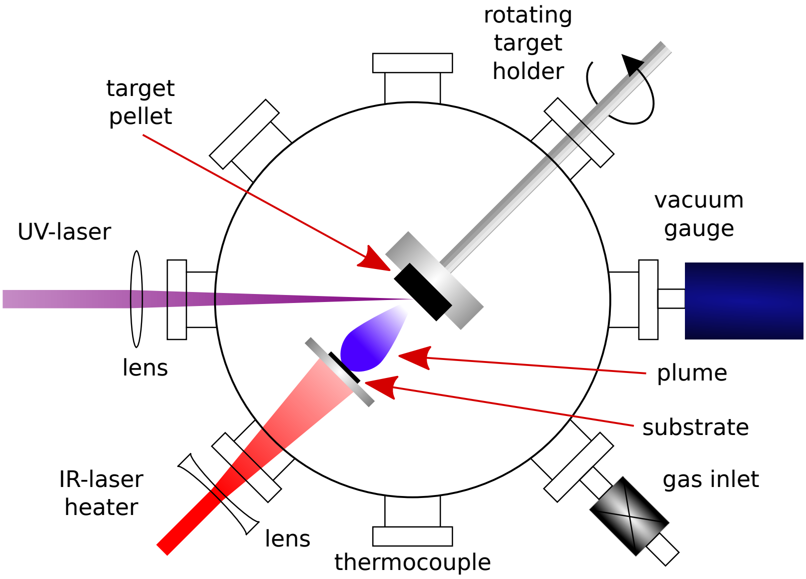

Figure 9. Schematic illustration of the pulsed laser deposition setup.

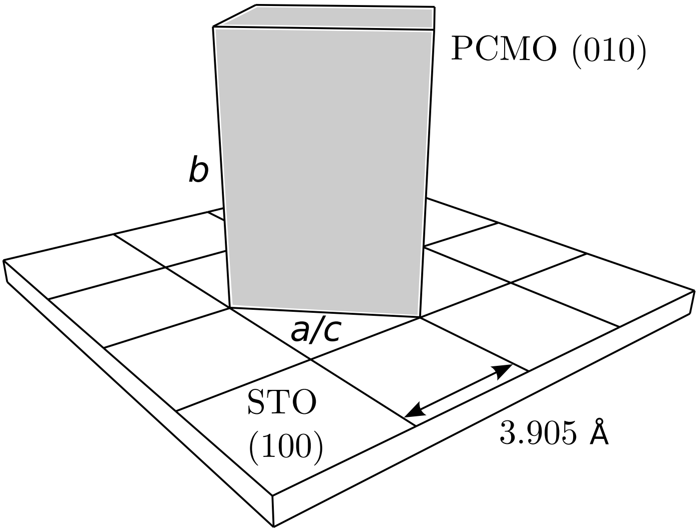

Figure 10. A schematic illustration of the growth direction of the PCMO film on top of the STO substrate showing 45° angle between the STO and PCMO lattices.

Table 1. Thickness and growth rate of the deposited films with different Ca concentration. [**P4**]

x	thickness (nm)	growth rate (Å/pulse)
0.3	100(2)	0.66
0.4	110(5)	0.73
0.5	125(6)	0.83

grow along the diagonal of the STO cube face ($a\sqrt{2} = 5.523$ Å) while the b parameter of PCMO is oriented out of the substrate plane, as can be seen from figure 10. As the bulk values of a and c parameters are smaller than in substrate it will induce an in-plane tensile strain on the PCMO film.

In this work, the ablation process of the thin films with varying Ca concentration x = 0.3, 0.4 and 0.5 was carried out at 500 °C where the substrate was heated with infrared laser at the rate of 25 °C/min. The flowing oxygen pressure in the chamber during the deposition process was p = 0.2 Torr. The used ultraviolet laser was an Excimer ASX-750 XeCl laser with a pulse repetition rate of 5 Hz and a duration of 25 ns with a laser fluence of 2 J cm^{-2}. The distance between the target and the substrate in the ablation chamber was 35 mm. In order to study the oxygen related effects on the thin films magnetic and transport properties, *in situ* post-annealing treatments under atmospheric pressure of pure O_2 were made either at T_a = 500 or at 700 °C for ten minutes with heating and cooling rates of 25 °C/min.

During the ablation process, 1500 ultraviolet laser pulses were shot to the target. The rate of the ablation process was confirmed with x-ray reflectometry of the prepared films. The increased Ca concentration increased the average growth rate being $\approx$ 0.66, 0.73 and 0.83 Å/pulse for x = 0.3, 0.4 and 0.5, respectively. The rate of the ablation process can be related with the increased porosity of the target with higher Ca concentration in this range, leading to more efficient vaporization [31, 32].

2.2 Structural characterization

The crystal structure and purity of the samples were investigated with x-ray diffraction (XRD). The symmetric lattice atoms of the investigated material scatter the x-ray photons which interfere with each other inducing a diffraction pattern which obeys the Bragg law [33].

As the quality of the targets is the essence of the PLD technique, the quality of the targets was confirmed straight from the surface of the target pellets by detailed 2θ XRD scans within the range of 20° - 70° using *Philips X'Pert Pro* diffractometer in the Bragg-Brentano configuration at room temperature with Cu Kα radiation, an incident 10 mm mask, 0.04 rad Soller slits and a programmable receiving slit and a 0.4 mm monochromator. The obtained XRD patterns were analyzed with the Maud-Rietveld refinement program [34].

The structural characterization of the film samples was made using Schulz texture goniometer with Nickel filter, 1x4 mm slit, 0.04 rad soller, 0.18° slit and a parallel beam collimator. The film quality was determined from 2θ scans in $(0b0)$ direction and 2D (ϕ, 2θ) scan of (031) peak which was chosen to avoid the overlapping of the diffraction peaks from the sample and the substrate.

2.3 Magnetic measurements

The magnetic measurements were executed using *Quantum Design* superconducting quantum interference device (SQUID) and physical property measurement system (PPMS) magnetometers. In both measurement systems, the sample is moved through pick-up coils such that the magnetization of the sample induces a measurable relative current in the coil.

In the SQUID magnetometer, the pick-up coil is inductively coupled to a superconducting ring with superconductor-insulator-superconductor type Josephson junction [35], where the magnetic flux through the ring induces a superconducting current in the ring which can be detected by an inductively coupled LC tank-circuit driven on radio frequency. The used SQUID magnetometer has superconducting magnets inducing a maximum of ±5 T magnetic field.

The PPMS magnetometer was operated with the ac measurement system option working as a vibrating sample magnetometer in the dc magnetization measurements. The PPMS system is also capable of measuring the ac magnetization, where the stationary sample is excited with the ac magnetic field and the magnetic response of the sample is measured with pick-up coils. All the ac magnetization measurements of the polycrystalline samples were done with PPMS magnetometer. The PPMS has superconducting magnets inducing a maximum of ±9 T magnetic field.

The temperature dependences of the zero-field-cooled M_{ZFC} and field-cooled M_{FC} dc magnetizations were measured using SQUID magnetometer for all the samples. For polycrystalline samples the temperature was ramped between 5 and 300 K under 8 mT dc field, whereas the thin films were measured at 20, 50, 100 and 150 mT external fields.

The magnetic virgin measurements at several temperatures and up to 9 T (5 T) were performed on the polycrystalline (thin film) samples with PPMS (SQUID) magnetometer, followed by the magnetic hysteresis loop measurements between ± 9 T (± 5 T) fields. In the magnetic virgin measurements, the external magnetic field is applied for the first time after cooling the sample from above the critical temperature to avoid the possible magnetic history of the samples. The thin film samples were always measured with external field B pointing along the planes of the films, i.e. along the PCMO [101] axis.

In the ac susceptibility measurements the real and imaginary components (χ and χ, respectively) were measured in the temperature range of 10 - 350 K in 1 K temperature steps and after that around thepeaks with 0.2 K temperature steps using a PPMS magnetometer with ac field of 1 mT and by varying dc fields between 0 and 50 mT and frequencies between 100 Hz and 10 kHz. All the measurements were made in the cooling direction.

The effect of static illumination to the magnetic properties of the thin films was measured with SQUID magnetometer with specialized sample holder and illumination setup. The M_{ZFC}, M_{FC} and virgin measurements were repeated in dark and under static illumination for $x = 0.4$ film sample with $T_a = 500$ °C.

2.4 Transport measurements

The magnetoresistive measurements for the thin film samples were carried out in PPMS magnetometer operating in resistivity mode and connected to the *Keithley 6487* picoammeter and the data was collected with Labview program. The thin films samples were connected with copper wiring as a standard two-point connection due to high resistivity of the samples and extensive resistivity range during measurements. The copper wires were soldered with indium on top of the film surface with 3.5 mm distance between them. The external field B of PPMS was pointing perpendicular to the plane of the films, i.e. along the PCMO [010] axis. The schematic illustration of the magneto-transport measuring setup is presented in figure 11.

During the virgin magnetoresistive measurements at various temperatures up to 8 T, the constant voltage of 200 V was used in the high resistivity regime down to 10^3 Ωcm. Between the resistivities of 10^3 Ωcm and 0.5 Ωcm, the measurement operates in constant current of 2 μA. At the resistivities below 0.5 Ωcm, the measurement turns back to the constant voltage mode using 0.1 V. The hysteresis loop measurements at various

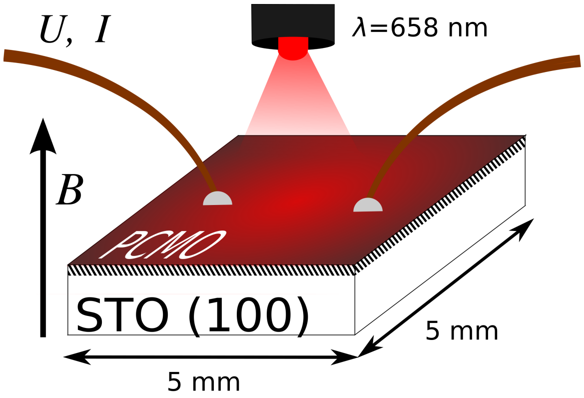

Figure 11. A schematic of the magnetoresistive measurement setup under illumination. [**P5**]

temperatures between ±8 T were made with constant voltage mode, as the resistivity range was greatly reduced, using suitable voltage for given sample and measuring temperature [**P5**]. However, in all the magnetoresistive measurements the current was always kept below 2 mA to avoid the colossal electroresistance effect [36].

2.4.1 Illumination setup

The illumination of the samples was realized with a home-made fiberoptic sample holder attached to the PPMS magnetometer where the laser spot covered the whole PCMO film. The experimental conditions were kept unchanged between the measurements in dark and under photoexcitation. The optical fiber from PPMS was connected to the AlGAInP laser diode emitting 658 nm (1.88 eV) with the maximum output power of 10 mW on the sample surface inducing the total maximum output density of ≈ 0.4 mW/mm^2.

The varying fluences were obtained by driving the laser diode with different currents. The laser output power for given current was measured from the PPMS end of the optical fiber with *Thorlabs S120VC* photodiode power sensor attached to *Thorlabs power meter PM100D*. The fluence measurements gave 55, 156, 258, 360, and 400 μW/mm^2 for the used currents.

The thin films' dynamical response to the illumination was studied with temporal measurements at 10 K under the various magnetic fields where the laser was switched on and off using different laser fluences. The voltage ranges of these measurements are reported in [**P5**].

3 Structural and magnetic proprieties of polycrystalline PCMO

3.1 Structural properties

The phase purity of the polycrystalline PCMO samples was confirmed using Rietveld refinement analysis on the XRD data measured at room temperature. The data did not show any impurity peaks and the refinement curves matched the collected data as can be seen from figure 12 where the diffractograms for all the samples are presented. The intensities of the first peaks of the diffractograms decrease with increasing Ca concentration which is in agreement with the decreasing amount of Pr in the samples. Also, the increased Ca concentration increases the intensities of four main peaks while diminishing the side peaks. This indicates that the distortion of the perovskite structure decreases when the amount of Ca is increased. This phenomenon is also observed from the evolution of the lattice parameters and unit cell volume with increasing x which are presented in the table 2, together with the goodness of the fit χ^2 and doping level obtained from the Rietveld analysis. With the increasing Ca concentration, the unit cell volume decreases and the lattice parameters a and c approach each other. This means that the crystal structure of PCMO turns from orthorhombic to more tetragonal, towards the ideal perovskite structure with increasing Ca concentration [37].

The decrease of the distortion of the perovskite structure with increasing Ca concentration can be explained with two different theoretical concepts. First, by replacing the Pr^{3+} with Ca^{2+}, the average ionic radius increases which reduces the deformity of the perovskite unit cell as the Goldschmidt tolerance factor [1] increases towards the ideal value of 1.0, according to the equation 1. Secondly, the hole doping concentration in PCMO is controlled by the amount of Ca which oxidizes the Mn^{3+} ions to Mn^{4+} ions. As the amount of Mn^{4+} ions increases in PCMO, the cooperative JT distortion breaks, generating only local JT distortions around Mn^{3+} ions. Hence, the increased hole doping reduces the JT distortion in the crystal lattice.

The temperature dependence of the crystal lattice structure of PCMO at low Ca concentrations without the CO phase [38] is very small. Nevertheless, for samples $x =$ 0.4 and 0.5, the crystal lattice changes from orthorhombic to monoclinic when the CO phase is reached upon decreasing temperature [21–23]. In the monoclinic structure there is more variation in the Mn-O bond lengths and Mn-O-Mn angles than in the orthorhombic phase due to the weakening of the continuous JT distortion.

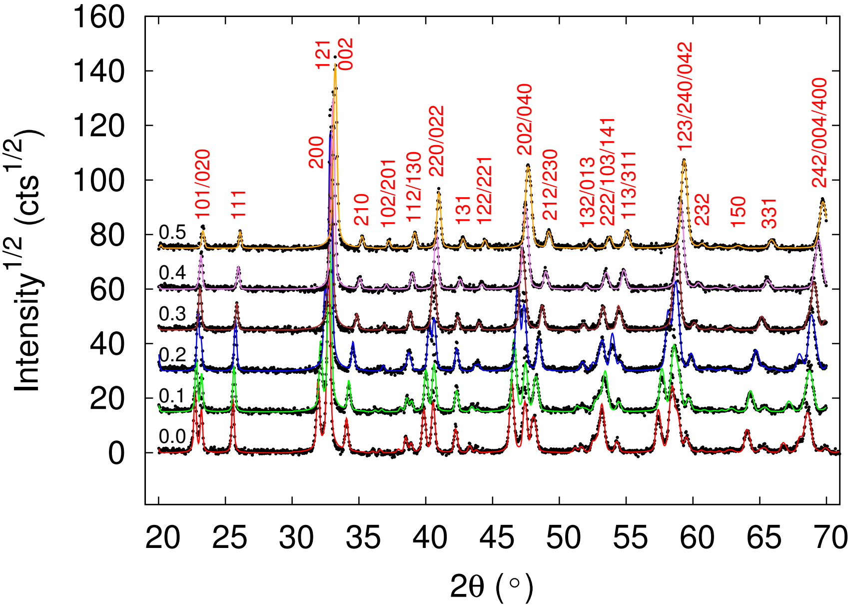

Figure 12. The measured XRD $\theta - 2\theta$ diffraction patterns with identified peak indices of the polycrystalline PCMO samples with varying Ca concentrations between $x = 0.0$ - 0.5. [**P1**]

Table 2. The lattice parameters, volumes of the unit cells, Ca concentration and the goodness of the fits χ^2 calculated from the XRD 2θ data for PCMO bulks with x between 0.0 and 0.5. [**P1**]

x	a (Å)	b (Å)	c (Å)	V (Å^3)	Ca concentration	χ^2
0.0	5.4617(5)	7.6656(6)	5.6020(4)	234.54(6)	-	2.19
0.1	5.4514(5)	7.6617(7)	5.5720(4)	232.73(6)	0.14(3)	2.44
0.2	5.5153(4)	7.6772(7)	5.4443(6)	230.52(7)	0.20(3)	2.99
0.3	5.4356(4)	7.6768(6)	5.4655(4)	228.06(6)	0.33(1)	1.61
0.4	5.4184(7)	7.6475(7)	5.4329(7)	225.12(8)	0.42(1)	1.43
0.5	5.3965(7)	7.6101(6)	5.4077(7)	222.08(8)	0.50(1)	1.37

3.2 Magnetic properties

3.2.1 Temperature dependence of magnetization

From the XRD analysis of the PCMO bulk samples, it was evident that controlling the charge distribution (Mn^{3+}/Mn^{4+} ratio) by varying the Ca concentration affects the continuous JT distortion and lattice parameters. Apparently, the effects of the Ca doping are even stronger on the magnetic properties of the polycrystalline PCMO, as can be seen from the temperature dependences of ZFC and FC (dc) magnetizations of all the samples presented in figure 13.

According to the neutron diffraction measurements by Jirak *et. al.* [37] all the samples show AFM ground state except in $x = 0.2$ which is found to be FM and in $x = 0.3$ which had coexistence of both AFM and FM phases. However, there is a large decrease of the FC net magnetic moment between samples $x = 0.3$ - 0.5, which cannot be explained with the doping induced increase of Mn^{4+} concentration. While the magnetic signal decreases in these $x = 0.3$ - 0.5 samples, a visible peak appears around 260 K indicating the onset of the CO and OO transition where the Mn spins start to couple, forming FM-chains [18, 39]. The CO peak amplitude becomes larger when the Mn^{3+}/Mn^{4+} ratio closes to 1:1 with the increasing calcium concentration. For sample $x = 0.3$ the peak is not visible at all but the small non-zero background signal at high temperatures indicates a weak charge and orbital ordering [**P1**].

The CO/OO phase is often described only for concentration $x = 0.5$ with charge exchange (CE) -type AFM structure shown in figure 14(a), where the coupling of the spins is AFM along the b-axis. When the carrier concentration in the system is increased by decreasing the calcium concentration, the extra electrons on Mn^{3+} sites hop along the b-axis mediating the FM double exchange interaction inducing canting of the spins in the b direction [5]. This induces a pseudo-CE-type AFM structure for $0.3 \leq x < 0.5$, where the spin arrangement along the b-axis becomes fully FM for $x = 0.3$, while the CE-type AFM order is maintained in ac-plane as shown in figure 14(b) [37]. This kind of evolution of AFM and FM interactions as a function of Ca concentration explains the observed effects in $M(T)$ measurements.

The AFM transition of the CO phase is visible in magnetic in-phase (dispersion) χ' ac susceptibility measurement around 170 K for samples $x = 0.4$ and 0.5 shown in figure 15, which is in good agreement with neutron measurements [37]. This indicates that the CO/OO phase builds up in wide temperature range between 260 - 170 K. For the sample $x = 0.3$, very complicated peak features are visible in magnetic out-of-phase

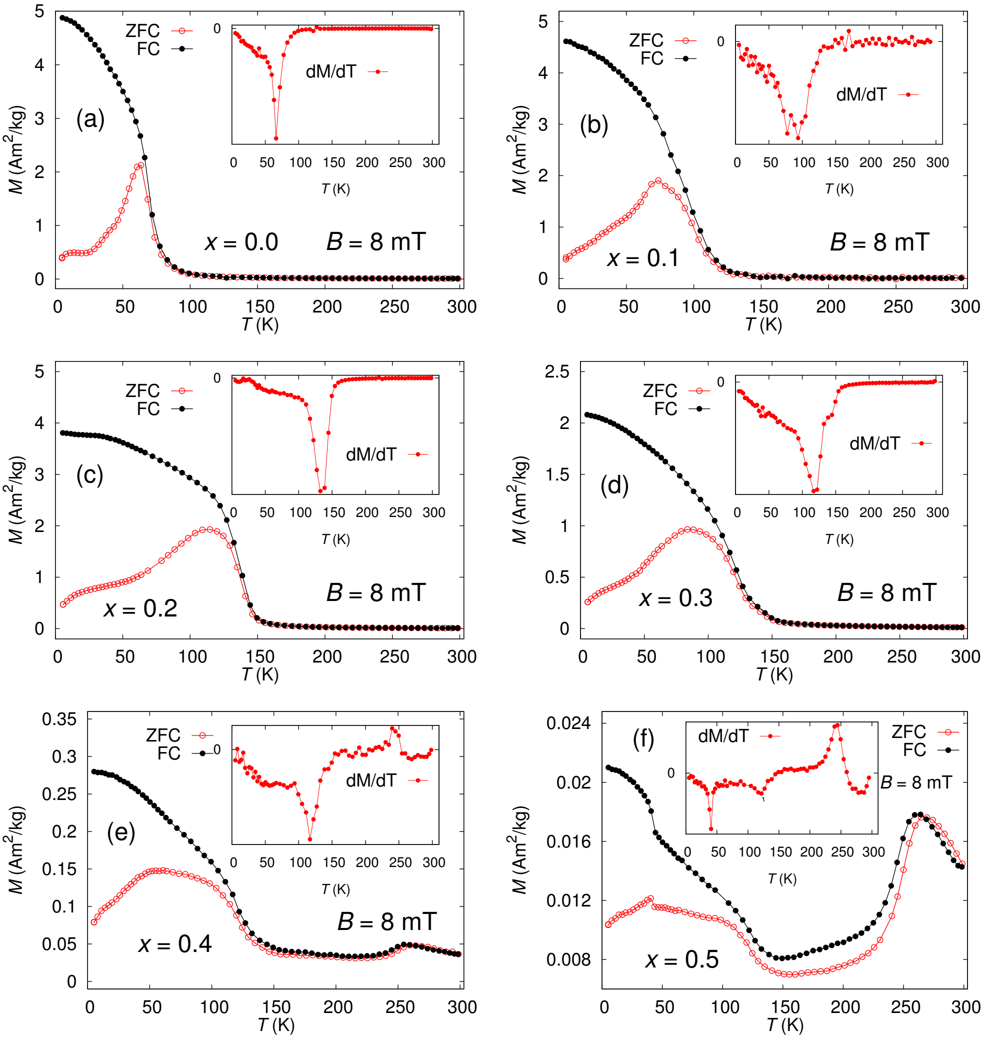

Figure 13. Temperature dependence of M_{ZFC} and M_{FC} curves measured with 8 mT external magnetic field for the PCMO bulks with varying Ca dopings between x = 0.0 - 0.5 (a) - (f). The insets shows the first derivatives of $M_{\mathrm{FC}}(T)$ curves where the minimum point indicates the magnetic transition temperature. [**P1**]

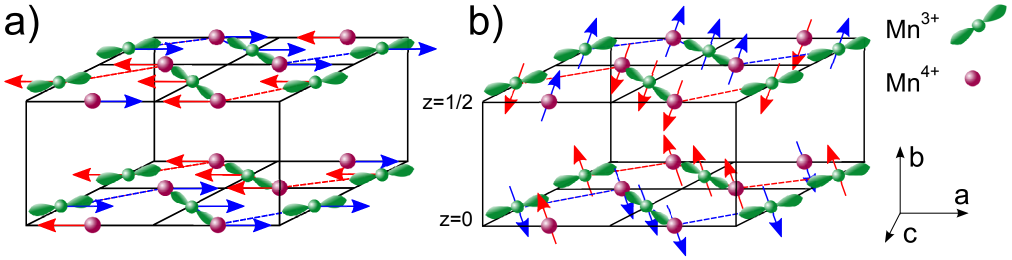

Figure 14. A schematic picture of antiferromagnetic (a) CE-type structure for $x = 0.5$ and (b) pseudo-CE-type structure for $x = 0.4$ with the pattern of CO/OO order on ac-planes. The antiferromagnetically coupled ac-planes of CE-type structure become ferromagnetically canted for pseudo-CE-type structure because of increased carrier concentration. [37]

(absorption) χ'' ac susceptibility measurement shown in figure 16, indicating coinciding AFM and FM transition in close temperature range around 140 - 110 K [**P2**]. The samples $x = 0.4$ and 0.5 have yet another magnetic transition around 120 K showing a large irreversibility between ZFC and FC dc magnetization curves in figure 13. There is no mention of this kind of low temperature transition in literature of neutron diffraction measurements for these $x = 0.4$ and 0.5 concentrations. For sample $x = 0.5$, there is also a large upturn around 50 K in FC magnetization curve, which indicates a magnetic impurity phase Mn_3O_4 (hausmannite).

The divergent behaviour between ZFC and FC dc magnetizations shown in figure 13 is not consistent with conventional second order magnetic AFM or FM phase transitions and it is actually found in all the samples below the low temperature transition. This phenomenon is called thermomagnetic irreversibility and in manganites it indicates magnetic phase separation or phase co-existence between AFM and FM clusters [40–42]. Below the temperature T_{irr}, where the ZFC and FC curves diverge from each oher, competing AFM and FM clusters exist in the system. Without the presence of the external magnetic field, the AFM coupled clusters dominate while under the magnetic field the amount of FM clusters is higher.

To get more insight of these complex low temperature magnetic phases, the ac susceptibility of the samples were measured [**P2**, **P3**]. For the samples $x = 0.0$ - 0.3, the temperature dependence of the χ'' ac susceptibility with several measuring frequencies and external magnetic fields are depicted in figure 16(a). In general, the magnitude of χ'' ac susceptibility signal is higher for samples with only single peak structure and smaller

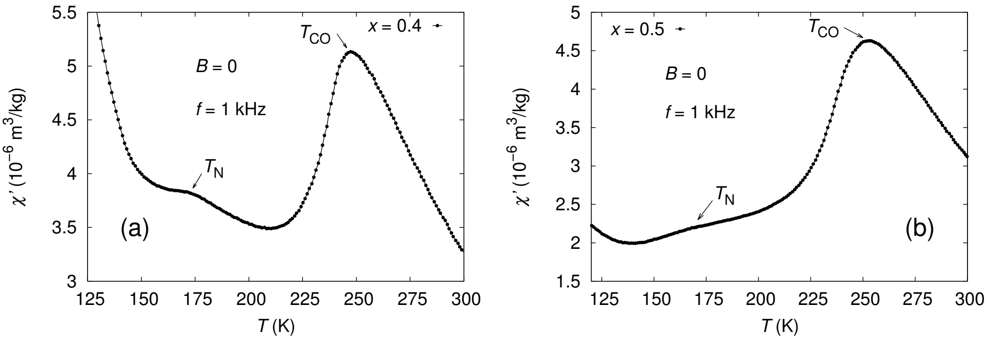

Figure 15. Enlarged view of temperature dependence of in-phase ac susceptibility χ' showing a small peak/shoulder around 170 K originating from AFM ordering for samples x = 0.4 and 0.5. The measurements were made with 1 kHz ac driving field frequency, 1 mT ac driving field amplitude and 0 mT external magnetic field.

for multiple peak structures. The highest amplitude is in the sample x = 0.2, which is in line with neutron diffraction measurements where the magnetic ground state of the sample was found to be FM. The χ'' susceptibility of the samples shows the evolution of the magnetic phases as a function of the Ca concentration, with many transition peaks in samples x = 0.1 and 0.3. The multiple peak structure of the χ'' ac susceptibility curves is in line with the neutron diffraction measurements, where these samples also showed a multiple magnetic phase transitions [37, 43].

The effect of the superimposed magnetic field to the susceptibility χ'' curve shape is the most dramatic for samples x = 0.0, x = 0.1 and x = 0.3. The peak intensity in the sample x = 0.0 is drastically reduced with an increased external dc field. Similarly, the lower temperature peak and the high temperature peak vanishes almost completely in samples x = 0.1 and x = 0.3,respectively, as depicted in figure 16b. This phenomenon indicates that these peak structures originate from similar AFM transitions. The transition peaks with FM nature are more resistant to the superimposed dc magnetic field. The lower intensity of the multiple peak structures can indicate that the whole sample is not in single magnetic phase and, hence, the whole sample does not take part in the transitions, which gives further evidence of the nanoscale phase separation and phase co-existence [**P2**].

The dynamical response of these magnetic transitions in samples x = 0.0 - 0.3 shows a temperature shift of the maximum position T_f of the χ'' peaks, as a function of the ac driving field frequency and external magnetic field, as can be seen in figure

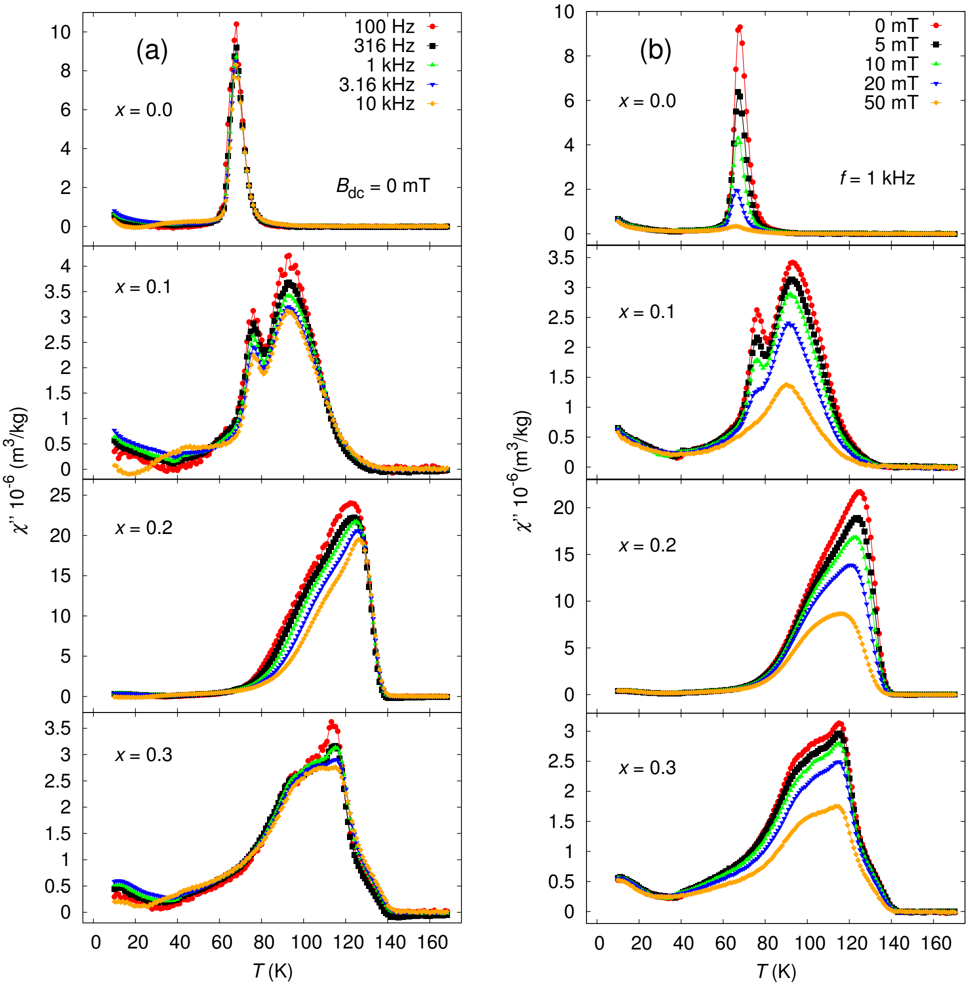

Figure 16. The out-of-phase ac susceptibility χ'' with varying (a) ac driving field frequencies f and (b) external dc magnetic field B_{dc} for PCMO bulk samples with $x = 0.0$ - 0.3. The used ac field amplitude h = 1 mT, (a) B_{dc} = 0 mT and (b) f = 1 kHz. [**P2**]

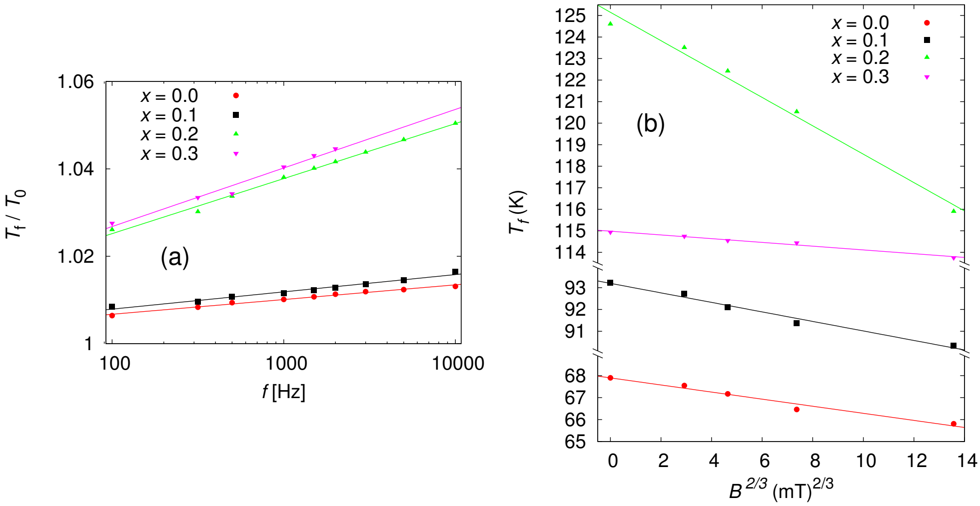

Figure 17. The variation of χ'' peak temperature T_{f} as a function of (a) frequency f and (b) external dc magnetic field B_{dc}. The solid lines are fitted to data points with equation (a) $\delta = \mathit{\Delta} T_{\mathrm{f}}/(T_0 \mathit{\Delta} \log f)$ [44] and (b) $B \propto (1 - T_{\mathrm{f}}/T_{\mathrm{g}})^{3/2}$ [46]. The scaling value T_0 and the spin glass freezing temperature T_{g} are the extrapolated peak temperatures at (a) $f = 0$ and (b) $B_{\mathrm{dc}} = 0$, respectively. [**P2**]

17. The peak temperature T_f increases linearly with the logarithm of the frequency, as shown in figure 17(a). Similar tendency is also found in samples x = 0.4 and 0.5 [**P3**]. This kind of T_f shift at low driving field frequencies is not visible for ordinary long range ordered materials [44]. Therefore, this is an indication of the frustrated magnetic system where it is not possible to arrange the FM and AFM couplings so that all the magnetic interactions are simultaneously satisfied due to the local geometrical limitations in the crystal lattice. Hence, there are magnetic phases that have the same or similar energy, which leads to multiple possible ground states [27, 44, 45].

From figure 17(a) it is evident that the T_f shift as a function of frequency becomes more significant with increasing Ca concentration, indicating that the frustration in the samples also increases with increasing Ca concentration between x = 0.0 - 0.3. According to the core-shell model, the manganite material with smaller particle size induces larger T_f shift with increasing frequency [47]. Hence, as the solid state reaction induces rather large particle size into our samples, the T_f shift is suppressed in our measurements. Another evidence for the existence of a frustrated glassy phase in our samples is the external magnetic field dependence of the T_f, as can be seen in figure 17(b). For samples $x = 0.0$ - 0.3, the decrease of the peak temperature T_f is linear with the superimposed magnetic field $B^{2/3}$. This behaviour is reported to be similar in a variety of spin and cluster glass materials [48–52]. Furthermore, the influence of the external magnetic field on the magnetic phase transition temperature indicates a first order magnetic phase transition, as the effect of magnetic field is comparable to the influence of the pressure on the structural first order transition.

From the ac susceptibility studies it can be concluded that the polycrystalline bulk samples show a frustrated behaviour between competing AFM and FM clusters with different magnetic exchange interaction, where the Ca concentration controls the amount of FM clusters and frustration in the sample.

3.2.2 Virgin magnetization and magnetic hysteresis

The further studies of the low temperature magnetic phase of the polycrystalline samples $x = 0.3$ - 0.5 revealed an interesting anomaly, as observed in the high magnetic field range of the magnetic virgin and hysteresis loop measurements $M(B)$ shown in figure 18(a). The virgin curves at 5 K show a sudden increase in magnetization after a certain threshold magnetic field. This anomaly can be explained with the external magnetic field induced first order metamagnetic transition from the AFM to FM phase, where the external magnetic field quenches the prevailing CO/OO phase and invokes the appearance of FM ordering. The threshold magnetic fields at 5 K for samples $x = 0.3$ and 0.4 are 3.5 and 5 T, respectively. For sample $x = 0.5$, the virgin curve shows only slight bending around 5 T field as the provided magnetic field of 9 T is not sufficient to induce the metamagnetic transition in this doping range [53, 54]. These threshold field values are in good agreement with the theory because with the increasing Ca concentration the Mn^{3+}/Mn^{4+} ratio approaches to 1:1 establishing a stronger CO phase.

After the virgin measurement at 5 K, the subsequent magnetic loop measurement from +9 to -9 T and back, the magnetization retraces a completely different path than the virgin curve for samples $x = 0.3$ - 0.5, suggesting training and spin memory effects. For sample $x = 0.3$, the loop measurement at 5 K shows only FM magnetization signal without any indication of metamagnetic AFM-FM phase transition. Also, the samples $x = 0.4$ and 0.5 show only a FM behaviour when magnetic field is reduced from ±9 to 0 T, but the metamagnetic AFM-FM is once again visible while the magnetic field is increased from 0 to ±9 T, inducing high field hysteretic openings to the loop measurement.

When the loop measurements are repeated at 50 K, the high field metamagnetic

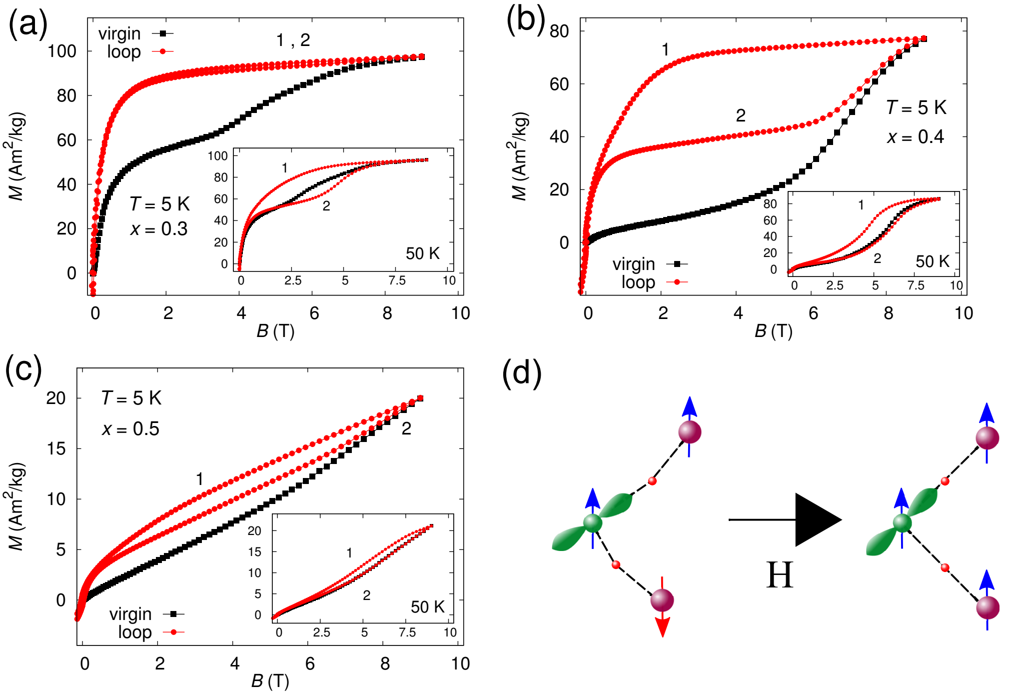

Figure 18. (a-c) The virgin curves and the positive field branch of hysteresis loops of polycrystalline PCMO samples with $x = 0.3$ - 0.5 measured at 5 K. The insets show the virgin and 1/4-loops measured at 50 K. (d) The straightening of the Mn-O-Mn bonds induces the metamagnetic transition under the increasing external magnetic field. [**P1**]

hysteretic behaviour appears also for sample $x = 0.3$ and the re-entrant FM-AFM transition becomes visible while the magnetic field is reduced from ±9 to 0 T for samples $x = 0.4$ and 0.5, as can be seen from the insets of figure 18(a-c). It is also evident that the threshold field for metamagnetic transition reduces at higher temperatures when the magnetic field is applied for the first time and the training effect diminishes as the loop measurement follows the virgin curve more closely. It seems that the stability of the CO phase *i.e.* doping concentrations and the magnitude of the applied magnetic field, determine the stability of the metastable FM phase at given temperature [**P1**]. For sample $x = 0.3$, the AFM-FM phase transition occurs only in one direction at 5 K showing non-hysteretic nature in loop measurements suggesting an irreversible process with the complete melting of the CO phase and achievement of full FM ordering. For samples $x = 0.4$ and 0.5, the provided magnetic field is not sufficient to establish the stable FM phase as the CO phase is not completely quenched and the two-directional reversible metamagnetic transition can be observed even at 5 K as a high field hysteresis of the loop measurement. With increasing temperature, the re-entrant transition from FM to AFM phase becomes more prominent for the sample $x = 0.4$ as the re-entrant FM to AFM transition becomes visible in the fist branch of the loop measurement. This indicates that the FM to AFM transition shifts to higher magnetic field range with increasing temperature which reduces the high field opening of the loop measurement [**P1**].

In the metamagnetic first order phase transition process, the application of high magnetic field induces torque to the spins and bends the distorted Mn-O-Mn bond angle towards 180° as schematically shown in figure 18(d). The increase of the Mn-O-Mn bond angles increases the electron hopping amplitudes and broaden the electron bandwidth W of e_g-band. Now, the mobilized e_g electrons make the ferromagnetic DE interaction more favourable between Mn^{3+} and Mn^{4+} ions, increasing the amount of FM clusters in the sample and inducing the metamagnetic AFM-FM transition. At the same time, the magnetic field induced modification of MnO_6 octahedra produces the first-order structural phase change [55]. From the metastable FM phase, the system does not destabilize itself back to its AFM ground state until the thermal energy in the sample is sufficient to provide extra entropy for the system to overcome a free-energy barrier [21].

4 PCMO thin films: Magnetic and magneto-transport proprieties under photo-illumination

4.1 Magnetic properties

The metamagnetic transition in the bulk samples with x = 0.3 - 0.5 is extremely interesting from a fundamental point of view and for its obvious potential for memory applications. Hence, it is very important to study how these kind of magnetical properties of correlated electron system can be transferred from bulk samples to the thin films. We found out that the crystalline PCMO x = 0.3 - 0.5 can be deposited on single crystal substrates using pulsed laser deposition technique at a low deposition temperature of 500 °C, which is significantly lower than the traditional deposition temperature of other complex oxides. For these films, two different *in situ* post-deposition oxygen annealing temperatures, T_a = 500 and 700 °C, were used to study the oxygen annealing effects on the magnetic properties of the films [**P4**].

The temperature dependences of ZFC and FC dc magnetizations are presented in figure 19 for films annealed at T_a = 500 °C and 700 °C for Ca concentrations x = 0.3, 0.4 and 0.5. All the samples show similar thermomagnetic irreversibility at low temperatures as observed in the bulk samples. The FC magnetization level at low temperature for the sample x = 0.3 annealed at 500 °C is five times higher than in the sample annealed at 700 °C. This difference in the saturation magnetization value between the samples with different annealing treatments decreases with increasing Ca concentration, having only limited effect on the samples with x = 0.5. Hence, the ferromagnetic phase volume seems to decrease with increasing annealing temperature in the samples with x = 0.3 and 0.4. Furthermore, in these samples, the magnetic transition also shifts to higher temperature with the increased FM ordering as can be seen from figure 19(d). For the x = 0.4 and 0.5 thin film samples, the height of the CO/OO peak is heavily suppressed and shifted to lower temperatures when compared with the bulk samples, indicating weaker CO phase stability in the thin films.

The strength of the CO phase was further investigated by measuring the virgin magnetization curves with the subsequent loop measurements between ±5 T magnetic field at different temperatures for all the samples. The positive field branches for measured curves are presented in figure 20. The characteristics of the metamagnetic AFM to FM transition are visible for the x = 0.4 and 0.5 films. On the other hand, neither of the samples with x = 0.3 show any metamagnetic transition at any temperature and only very limited high field hysteresis, indicating the nonexistence of the AFM CO phase.

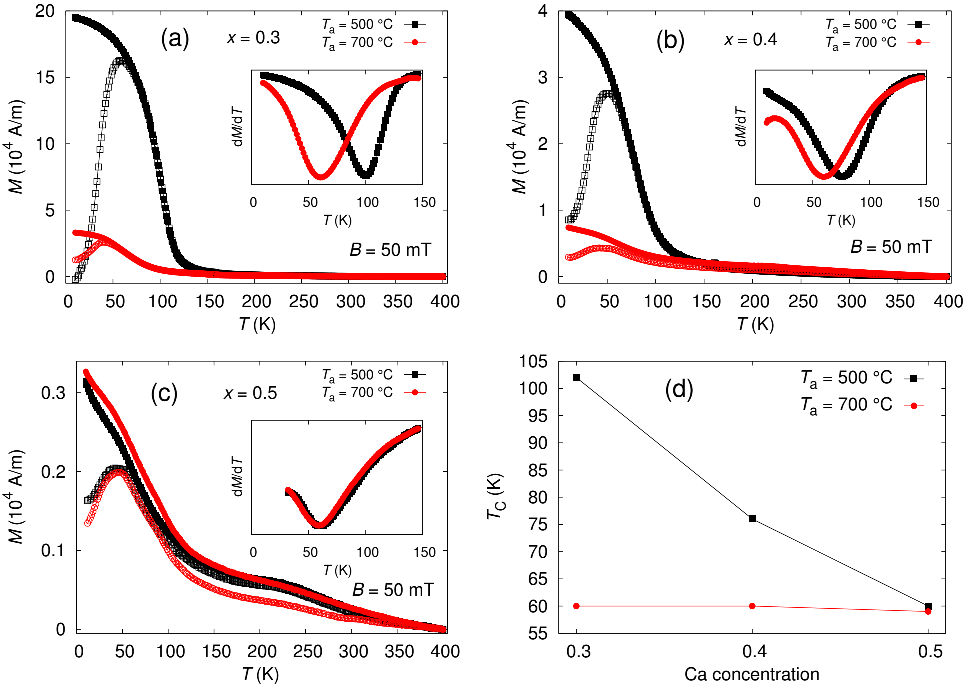

Figure 19. Temperature dependence of the M_{ZFC} and M_{FC} magnetizations with $B =$ 50 mT for differently annealed samples at $T_{\mathrm{a}} =$ 500 and 700 °C for Ca concentrations $x =$ 0.3 - 0.5, (a)–(c), respectively. The insets show the first derivatives of M_{FC} curves. The thin films transition temperature T_{C} as a function of Ca concentration (d). **[P4]**

Similarly, the threshold magnetic field for the metamagnetic transition in the $x = 0.4$ and 0.5 films is much lower and the transition steeper than in the bulk samples with the same Ca concentrations.

There are also huge differences in the virgin-loop measurements between the thin film samples with different annealing treatments. Thin films with $T_\mathrm{a} = 500$ °C show greatly reduced metamagnetic transition field and lower CO phase melting field compared to the samples with $T_\mathrm{a} = 700$ °C. This indicates weaker CO phase in the samples annealed at 500 °C. These observations are well in line with the $M(T)$ measurements where the lower annealing temperature increased the FM ordering of the samples. Therefore, the improved ferromagnetic interaction in thin films annealed in oxygen at 500 °C destabilizes the CO phase and, hence, it can be quenched with a considerably low magnetic field [**P4**]. This finding of the CO phase formation on thin film with considerably reduced magnetic field for the metamagnetic transition in samples with $T_\mathrm{a} =$ 500 °C is a very promising result from the technological point of view.

4.1.1 Effect of static illumination

The magnetic measurements were repeated in dark and under illumination for $x = 0.4$ $T_a = 500$ °C thin film sample, as presented in figure 21. In the M_ZFC and virgin-loop measurements the sample is cooled in dark and the light is turned on at the beginning of the measurement. In the M_ZFC measurement, the initial level of magnetization in the sample at 5 K is higher when compared to the measurement in dark. Also, in the virgin-loop measurement at 10 K, the saturation magnetization and the difference between the virgin and the loop measurement curves are higher under illumination. This indicates that the illumination increases the amount of FM clusters in the sample, which in turn intensifies the metamagnetic transition in the used magnetic field range. However, the effect of illumination diminsh in the M_FC and virgin-loop at 70 K measurements. This indicates that the effects of temperature and illumination have similarities which are properly discussed in the magnetophotoresistance section.

4.2 Structural analysis

The weaker CO phase in the thin films when compared with the bulk samples is very common phenomenon in the colossal magnetoresistive manganites. The changes in CO phase stability in thin films are often explained by the strain effects, where the substrate induced tensile strain increases the Mn - O - Mn bond length and stabilizes the CO phase, whereas the relaxation of the strain increases the FM ordering of the samples

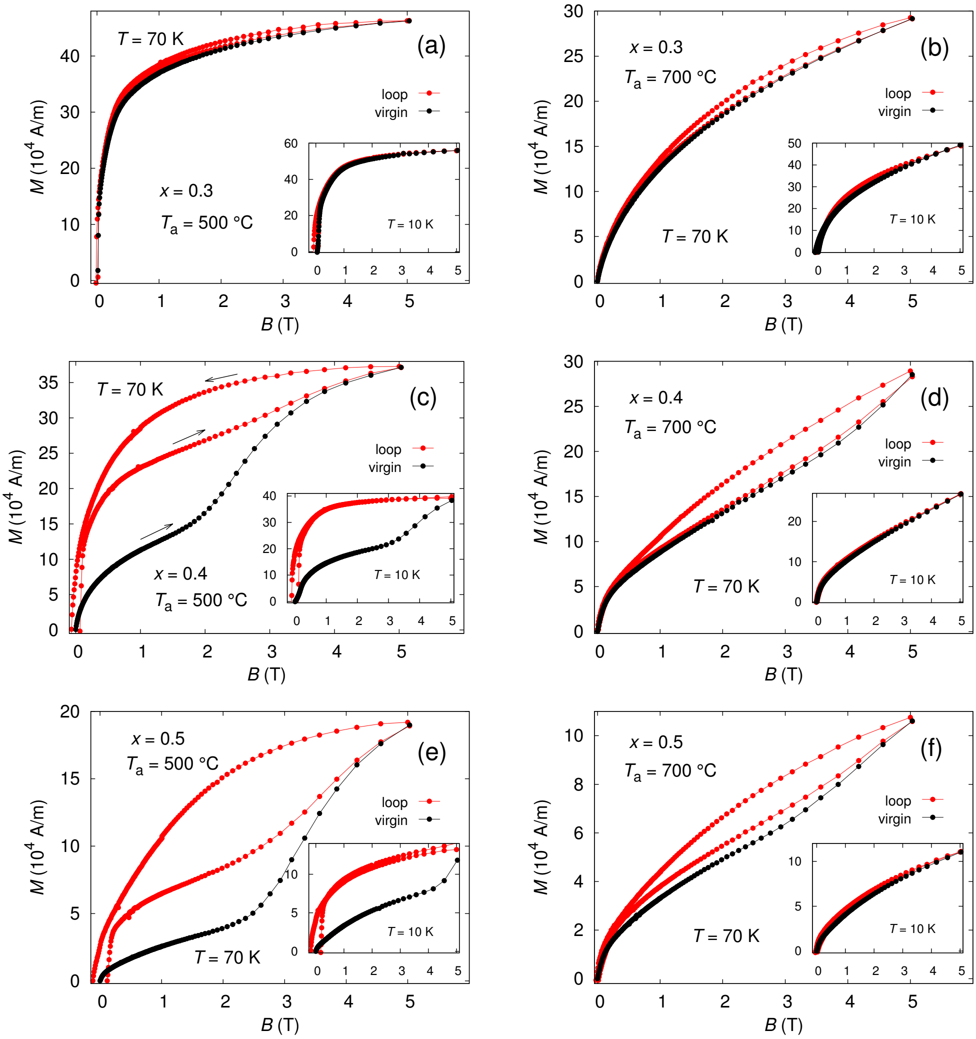

Figure 20. The positive field branches of the magnetic hysteresis loops with the virgin curves of $x = 0.3$ - 0.5 Ca-doped PCMO thin films measured at 70 K and at 10 K (insets) showing metamagnetic behaviour at different magnetic field ranges. (c) The magnetic field ramping directions. [**P4**]

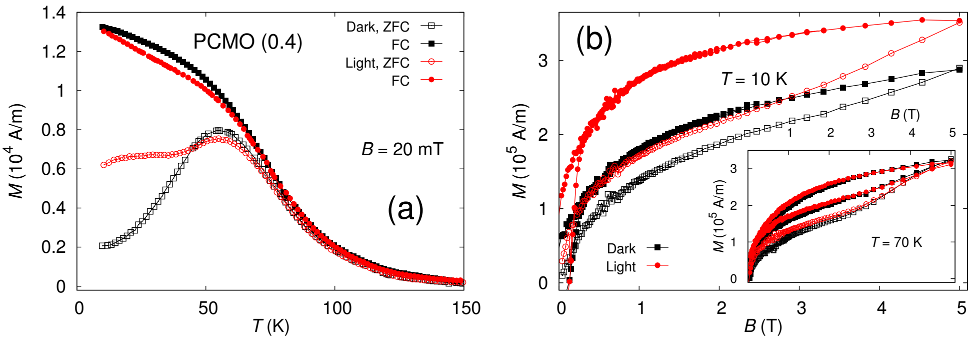

Figure 21. (a) Temperature dependence of magnetization and (b) positive field branches of the magnetic hysteresis loop with the virgin curve of $x = 0.4$ $T_a = 500$ °C film sample.

[56–59]. This stabilizing effect of the substrate induced tensile strain is understandable, as the melting transition of CO state is of the first order and accompanied with an actual change in crystal lattice symmetry [60]. Hence, the substrate induced strain supports the prevailing lattice symmetry stabilizing the CO phase and increasing the required field for metamagnetic transition. This means that the robust bulk like CO phase is achieved in the very thin films that have large substrate induced strain. This is a problematic concept because the CO phase stability of the film is closest to the bulk sample when the influence of the substrate is strongest [58, 59]. However, the report of Zhang *et al.* shows that the CO phase weakens with the decreasing particle size, due to the increased relative ratio of the FM coupled surface spins in the particle [47]. This would explain the weaker CO phase in relaxed thin films with smaller grain size when compared with the bulk samples. Furthermore, the high-angle grain boundaries and crystal defects in the polycrystalline bulk samples can act as pinning sites, interrupting the phase transition and increase the stability of the CO phase.

The structural analysis was done to the thin film samples to study the effects of the oxygen annealing treatment. The measured $\theta - 2\theta$ scans of the thin films showed only $(0b0)$ peaks of PCMO indicating that all the films were phase pure and b-axis oriented [**P4**]. Also, similarly as in bulk samples, the unit cell volume of the thin films was reduced with increased Ca concentration. Quite surprisingly, all the thin film samples treated at lower temperature $T_\mathrm{a} = 500$ °C showed narrower peak structure in both angle directions in the ϕ- and 2θ-measurements of the (031) peak as can be seen from figure 22 (for $x = 0.4$). The broadening of the peak in the samples with $T_\mathrm{a} = 700$ °C is clearly

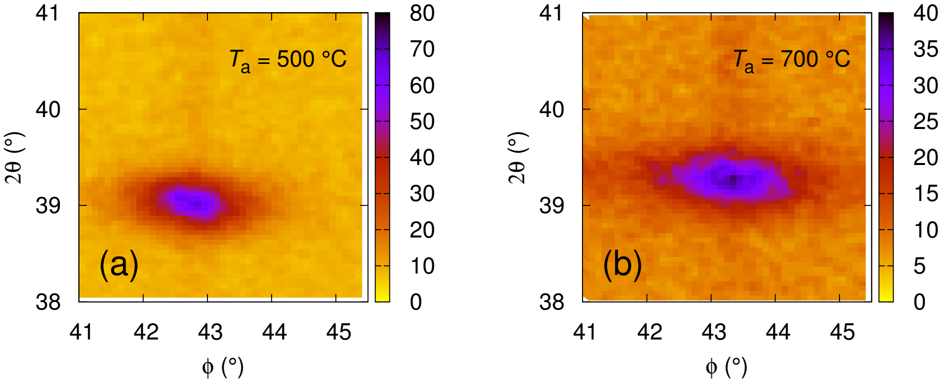

Figure 22. The ϕ - 2θ XRD measurements for (031) peaks of the $x = 0.4$ film annealed at (a) 500 and at (b) 700 °C. Note that the ϕ and 2θ scales are the same in both cases unlike the out-of-plane color scales. [**P4**]

more pronounced in ϕ-direction. Also, the peak amplitude of the film annealed at 500 °C is nearly twice as high as in the film with $T_{\mathrm{a}} = 700$ °C, but the integrated intensities are almost equal. The FWHM values of the (031) peak indicate that the films oxygen annealed at 500 °C have a better ordered and relaxed crystal structure with less random crystalline defects, while the samples with oxygen annealing temperature at 700 °C have low angle grain boundaries and in-plane lattice distortions inducing more random strain in the film [**P4**].

The higher amount of random strain in the films annealed at 700 °C is well consistent with the reduced ferromagnetism and the higher CO phase melting field in these samples. However, the random strain in these samples is induced by low angle grain boundaries and in-plane distortions of the lattice and does not directly result from the substrate induced strain. Therefore, such large differences in the magnetic properties between the samples cannot be solely explained by the random strain. The low temperature oxygen annealing treatment at 500 °C reduces the amount of oxygen in the film sample, increasing the Mn^{3+} ion content. This reduces the ratio of the Mn^{3+}/Mn^{4+} ions having similar effect on the thin films as the decreasing of the Ca concentration had in the bulk samples [**P4**]. Hence, the low temperature *in situ* post-annealing treatment increases the FM interaction in thin films, at the same time reducing the CO melting field dramatically. The robust AFM CO ground state in the thin films treated at higher temperature indicates that either the increase of the Mn^{4+} ion content or the randomly

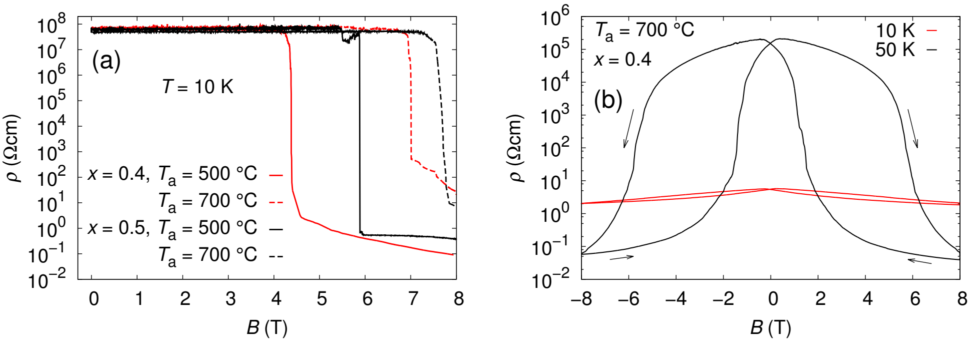

Figure 23. (a) The magneto-transport virgin measurements for the thin film samples $x = 0.4$ and 0.5 with both annealing treatments at 10 K [**P4**]. (b) The magnetoresistive loop measurements for thin film $x = 0.4$ with $T_\mathrm{a} = 700$ °C measured at 10 and 50 K.

distributed structural defects and strain enhances the CO phase.

4.3 Magneto-transport properties

In order to investigate the electronic transport properties of the metamagnetic transition and melting of the CO phase, the magneto-transport measurements were done with the PCMO thin films that showed a clear CO phase in the magnetic measurements *i.e.* samples with $x = 0.4$ and 0.5. As can be seen from figure 23(a), the virgin curve of the resistivity shows a colossal drop under the external magnetic field for thin film samples of both concentrations, indicating a magnetic field induced IMT. When the virgin measurements were repeated at higher temperatures, the IMT became wider and the CMR effect slowly decreased. Also, the required magnetic field for IMT decreased with increasing temperature like earlier observed in magnetic measurements in the threshold field for the metamagnetic AFM to FM transition.

The magneto-transport loop measurements at 10 and 50 K are presented only for thin film sample $x = 0.4$ with $T_\mathrm{a} = 700$ °C in figure 23(b) because all the measured samples showed similar behaviour. The change in resistivity in the loop measurements at 10 K is greatly reduced as all the measured samples stay in the metastable metallic phase with low resistivity range, indicating irreversible IMT process at this temperature. However, a colossal change in resistivity with a large hysteresis effect is observed in the loop measurements at 50 K as the samples return to the insulating phase. This observation, where the loop hysteresis in high field range increases with increasing temperature, is exactly similar as previously observed in the magnetic loop measurements, indicating that the metamagnetic AFM to FM transition and the melting of the AFM CO phase are closely related to the IMT. Hence, the external magnetic field induces AFM to FM phase transition and consequently increases the hopping amplitude of the e_g electrons leading to an insulator to metal phase transition and a CMR effect.

From the magneto-transport virgin measurement, we can conclude that the *in situ* annealing treatment has a large effect on the IMT fields of the thin films as the required magnetic field for IMT is smaller in the thin films treated at 500 °C than in the ones with $T_\mathrm{a} = 700$ °C. This is again in agreement with the magnetic measurements. For the samples with $x = 0.4$, the change in oxygen annealing temperature from 700 to 500 °C reduces the IMT field by 37% from 7 T to 4.4 T. Correspondingly, for the samples with $x = 0.5$, the required field for IMT is reduced by 22% from 7.6 T to 5.9 T due to lower oxygen annealing temperature. Hence, as the IMT field strength is proportional to the strength of the CO phase; the samples with $x = 0.5$ show a stronger CO phase compared with the $x = 0.4$ counterparts with higher $\mathrm{Mn}^{3+}/\mathrm{Mn}^{4+}$ ratio. Also, the $T_\mathrm{a} = 500$ °C films with the lower IMT fields show a larger resistivity switch of almost nine orders of magnitude within the limits of measuring accuracy, when compared with the films treated at 700 °C with higher IMT field, whose resistivity drop is around six orders of magnitude in the measured magnetic field range. Also, the higher minimun resistivity value at the 10 K loop measurement compared with the 50 K measurement in figure 23(b) can be explained with insufficient magnetic field range at 10 K, which cannot completely turn the sample into the metallic phase. We can conclude that with the combined effect of hole doping and oxygen annealing treatment, it is possible to produce various $\mathrm{Mn}^{3+}/\mathrm{Mn}^{4+}$ ratios inducing a wide range of IMT fields between samples and hence different strengths of CO phases [**P4**].

5 Magnetophotoresistance

5.1 Static illumination

In order to harness the full potential of the IMT in the CMR manganites, it is important to study how the transition can be driven more efficiently. Hence, the transport measurements were done under illumination to increase the functionality of the thin film samples and to investigate the combined effect of the magnetic field and illumination on the electrical properties of the PCMO thin films. The samples for measurements under illumination were selected to have maximum difference between the CO phase strengths. Hence, the films $x = 0.4$ with T_a = 500 °C called p40-500 and $x = 0.5$ with T_a = 700 °C called p50-700 were selected for further study.

The performed virgin magnetoresistive measurements under continuous illumination and in dark at 10 K are presented in figure 24(a-b) showing that illumination reduced the magnitude of the magnetic field required to induce IMT in both samples. The transition field decreases by 50% under the illumination, from 4.4 T to 2.2 T, for sample p40–500 and by 27%, from 7.6 T to 5.5 T, for sample p50–700. We called this joint effect of light and magnetic field on the samples resistance as the magnetophotoresistance [**P5**].

The temperature dependence of illumination effect on IMT was studied by repeating the virgin measurements at several temperatures as shown in figure 24(c) for sample p40-500. The effect of illumination on the IMT field diminishes as the temperature gets closer to the critical temperature, and the effect is almost zero at 50 K for both samples. The effect of illumination on IMT field vanishes at 80 K while the overall CMR effect is also reduced as can be seen from figure 24(d). The change of the CMR effect is over 5 decades for the p40–500 sample and only 2 decades for the p50–700 sample. This indicates that the illumination effect to the IMT field is prominent below T_irr where the magnetic phase separation between FM and AFM is evident. The IMT fields with and without illumination are presented in the inset of figure 24(b) for both samples. The transition field decreases steeply in dark when the temperature is increased to 50 K for both samples, whereas under illumination the transition field increases moderately for sample p40–500 and decreases slightly for sample p50–700 in the same temperature range.

The influence of illumination on the IMT field was further studied with virgin measurements at 10 K using several different laser fluences. From figure 24(e), it can be seen that even a few lowest laser fluences have an immense reduction to the IMT field.

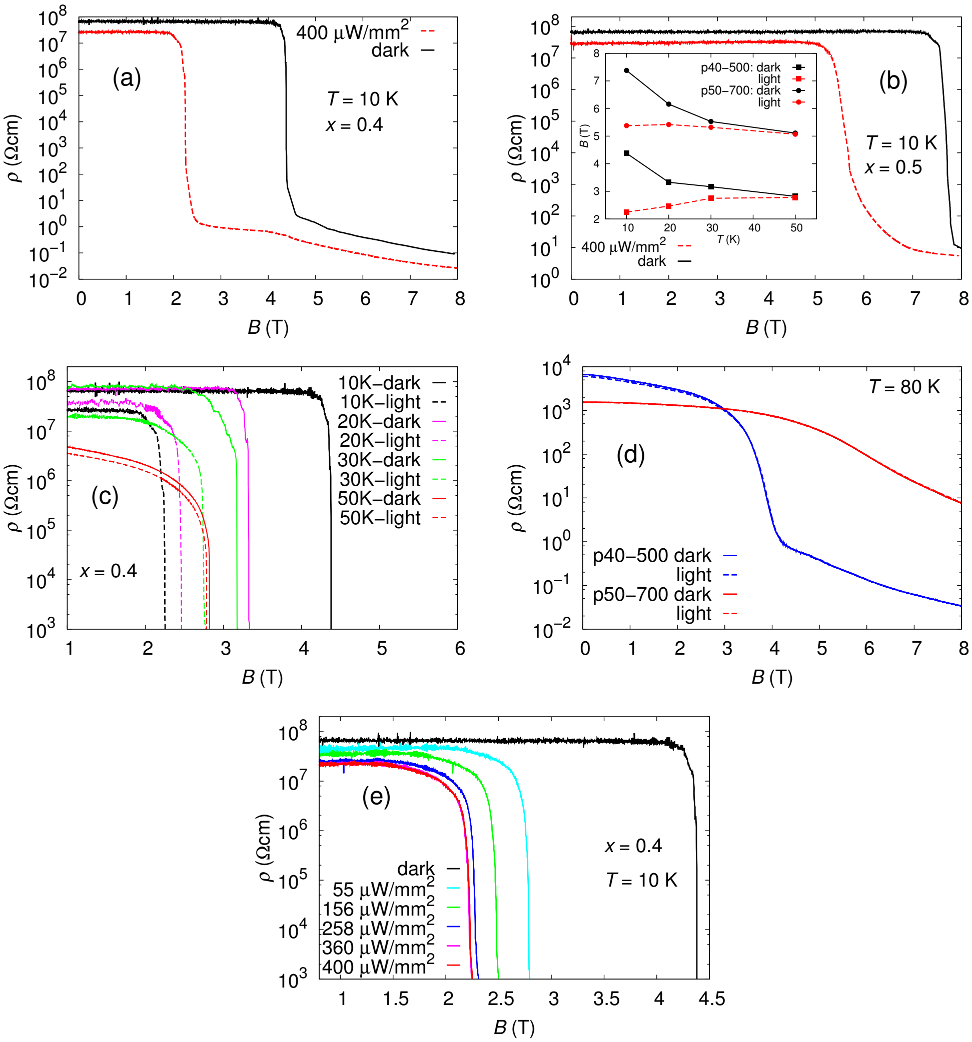

Figure 24. The magnetoresistive virgin measurement at 10 K in dark and under illumination (400 μW/mm^2) while the background magnetic field is risen to 8 T for both samples (a) p40–500 and (b) p50–700. (c) Virgin measurement repeated at various temperatures in dark and under illumination (400 μW/mm^2) for sample p40-500 [**P5**, SI]. (d) Virgin measurement repeated at 80 K in dark and under illumination (400 μW/mm^2) for both sample. (e) Repeated virgin measurement at 10 K with varying laser fluences for sample p40–500. The inset of (b) represents the temperature dependence of IMT field in dark and under illumination for both samples. The IMT field is calculated from the point where a sharp drop of resistivity starts. [**P5**]

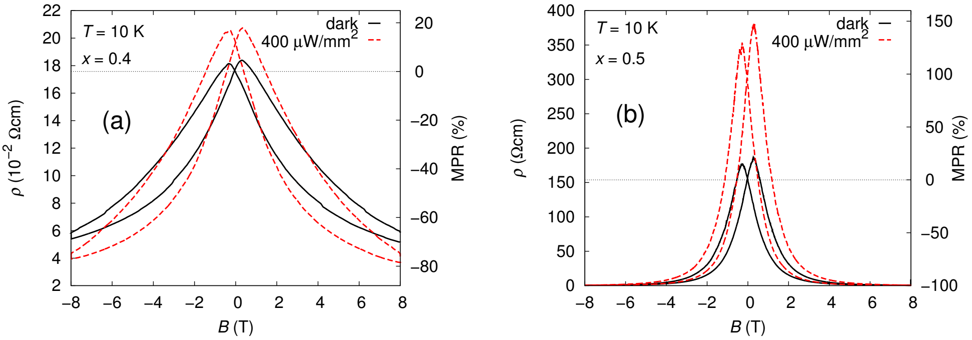

Figure 25. Magnetoresistive loop measurements at 10 K measured in dark and under illumination for both samples (a) p40–500 and (b) p50–700 with calculated magnetophotoresistance (MPR) percentages $[(R_{\mathrm{H}} - R_{0\mathrm{T-dark}})/R_{0\mathrm{T-dark}}] \cdot 100\%$. [**P5**]

The effect is similar on both samples where the IMT field decreases as the laser fluence is increased [**P5**]. The changes in the IMT fields between low fluence values are prominent but the effect slows down as the fluences are further increased, indicating the saturation of the fluence effect at higher fluences.

The illumination and the increasing temperature have very similar effects on the transition field and, hence, we have to exclude the effect of laser-induced heating of the sample. There are few observations which prove that the observed effects are indeed due to the illumination and not due to the heating. Firstly, for sample p40–500, the lowest transition field is achieved by illuminating and not by heating the sample. Also, if the samples would heat up with the laser light, the initial resistivity level of the virgin curves should also be reduced similar to that of the curve measured at 50 K. Moreover, already a very low fluence of 55 μW/mm^2 has an immense effect on the IMT field. The possible heating effect of the sample has also been thoroughly analyzed in the supporting information of [**P5**]. Hence, we can conclude that the sample heating effect is insufficient to solely explain the observed illumination effects.

The magnetoresistive loop measurements were also performed in dark and under light at several temperatures. The effect of illumination is clearly weaker in the loop measurements in comparison to the virgin measurements. However, the illumination effect reduces with increasing temperature. Also, the maximum effect of illumination is achieved at 10 K for both samples as can be seen from figure 25. It seems that in the metastable FM-metallic phase, when the magnetic field is turned back to zero, illumination seems to push the samples to a comparatively higher resistance phase. In addition, the effect of illumination seems to be more pronounced in the sample p50–700, indicating more persistent metallic phase in sample p40–500 than in sample p50–700 in the used external magnetic field range. The reason for this is probably the used applied magnetic field range of 8 T that is barely enough to induce the IMT in sample p50–700, whereas it is well beyond the required field for IMT in sample p40–500. Therefore, the used 8 T field is not sufficient to completely lock the metastable metallic phase in sample p50–700. This also indicates that by controlling the magnetic field range the stability of the metastable metallic phase can be controlled [**P5**].

5.2 Temporal illumination

The temporal resistivity measurements were done to study the dynamic response of resistivity while switching the illumination on and off. The measurements were performed in three different situations where the magnetic history of the sample was different. All the three cases are measured at 10 K and presented only for sample p50-700 in figure 26 as the differences between samples are minimal. In the first case of the temporal resistivity measurement, the sample is at the insulating phase without an external magnetic field and, hence, the effect is termed photoresistance (PR). The reduction of resistivity upon illumination is observed for both samples and the effect is strongly dependent on the laser fluence, being larger for higher laser fluences with maximum of almost 60% for p40–500 and 80% for p50–700 [**P5**]. This indicates that the illumination alone does not induce IMT, as the maximum resistivity drop is less than a decade. The resistivity response to the switching of illumination is very fast, indicating a normal semiconductor like transient photoconductivity where the carriers are excited across the bandgap by illumination. Therefore, this process increases the free electron and electron hole concentration [61].

In the second and third case of the temporal resistivity measurements, the sample is at the metallic phase in the presence of 9 T and 0 T magnetic fields, respectively, as depicted in figure 26(b - c). The observed resistive response to light for both samples is different when compared with the insulating phase. Under the 9 T magnetic field, the illumination still reduces the resistivity, but when the magnetic field is reduced to zero, the increase of resistivity upon illumination is observed. In both cases the light drives the system towards the minimum energy state depending on the prevailing magnetic field. These effects are in line with the loop measurements data in figure 25. In both cases, the time dependent change in resistivity is slower than in the insulating phase. Also, the effect of light is persistent in both cases as the switching off the illumination

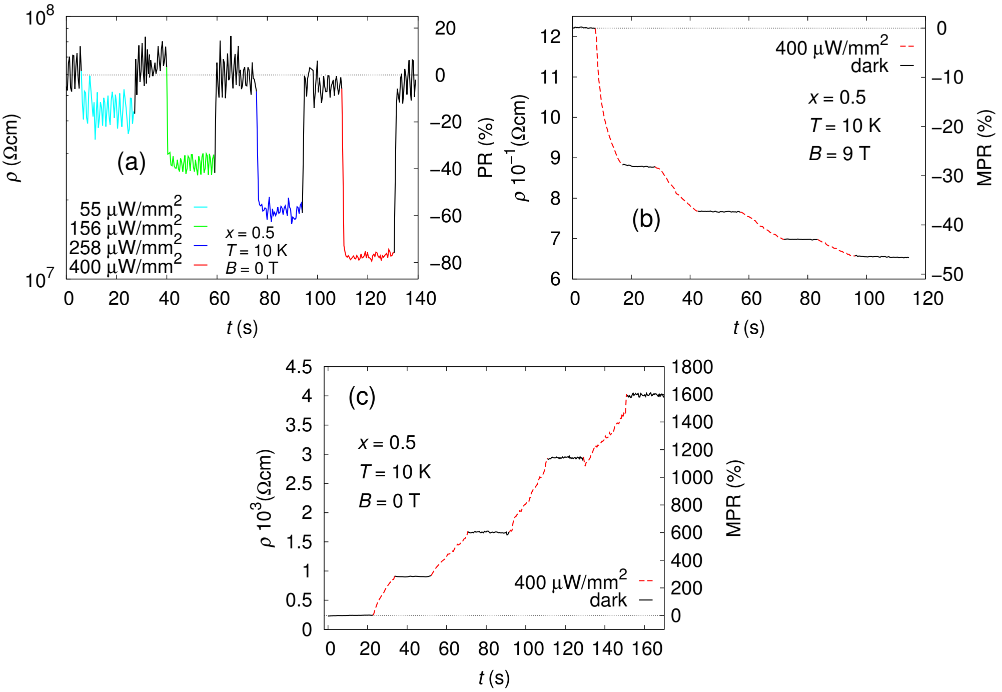

Figure 26. The temporal resistivity response to illumination measured at 10 K for sample p40–500, where the black colour indicates the sample without illumination. (a) Measured at the insulating phase without an external magnetic field with several laser fluences [**P5**]. (b) Measured at the metallic phase under 9 T external magnetic field using 400 μW/mm^2 laser fluence. (c) Measured at the metallic phase after the magnetic field was reduced from 9 T to zero with laser fluence of 400 μW/mm^2. The graphs show also the calculated photoresistance (PR) and magnetophotoresistance (MPR) percentages $[(R_{\text{ill.}} - R_{\text{dark}})/R_{\text{dark}}] \cdot 100\% \cdot$ [**P5**, SI]

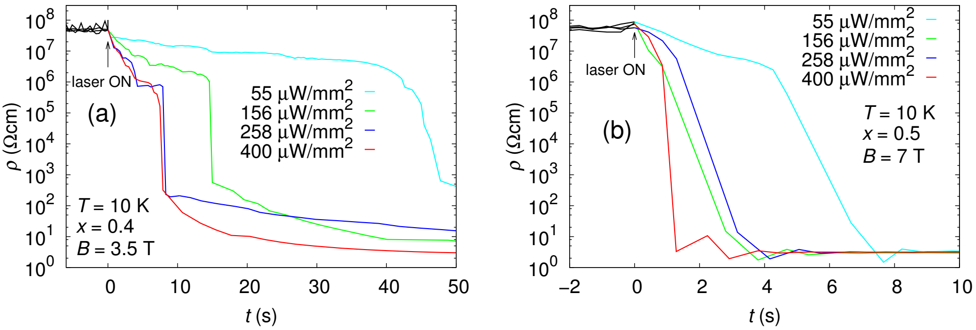

Figure 27. The temporal resistivity response to illumination measured for magnetically biased samples (a) p40–500 and (b) p50–700 under the 3.5 and 7 T, respectively, background magnetic fields at 10 K with different laser fluences. The black color indicates the sample without illumination. [**P5**]

does not revert the resistivity to the initial value. This indicates that in the metallic phase the resistivity can be changed as a function of the exposure time of light [**P5**]. However, the intensities of these effects are reduced with longer exposure time.

5.3 Magnetic biasing

The most significant light induced effect was achieved by the magnetic biasing of the sample where the background magnetic field is set between the IMT fields measured in dark and under illumination. The colossal effect of IMT is observed upon illumination of samples under magnetic biasing at 10 K as the resistivity switch in both samples is around seven decades (figure 27). It also seems that the duration of the complete IMT transition is dependable on the relative strength of the biasing magnetic field compared with the transition field value in dark. The closer the magnetic bias field value is to the transition field value in dark, the faster the transition occurs when illuminated. Also, it is evident that with the lower used laser fluence the IMT occurs slower. Therefore, the light intensity induced IMT could be fine-tuned with the illumination fluence, exposure time and background magnetic field. However, this transition was also persistent, as the switching of the illumination did not return the sample to the insulating phase. To explain all these observed light induced effects, we have to consider the nanoscale phase separation in the manganites, which will be discussed in detail in the next section.

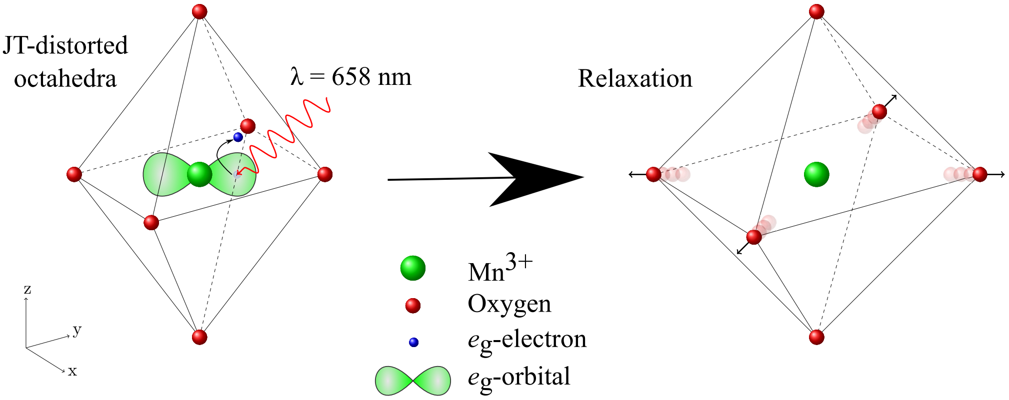

Figure 28. A schematic illustration of the photoexcitation of the Mn^{3+} e_g electron. Photoexcitation induces a relaxation of the JT distortion of the MnO_6 octahedron generating a lattice vibration.

5.4 Mechanism of magnetophotoresistance

In PCMO, the CO phase is strongly coupled to the lattice via the orbital degree of freedom that rises from JT distortion [62]. This means that the e_g electron in the Mn^{3+} site induces a lattice distortion to a surrounding oxygen octahedron. When the e_g electron moves through the lattice, the lattice distortion follows it from one octahedron to another, inducing a lattice vibration called phonon. Together this kind of dynamic electron–phonon interaction leads to the formation of polaron. When the PCMO samples are exposed to illumination, the 1.88 eV photons excite the Mn^{3+} intrasite transition where the electrons hop from e_{g1}-orbitals to e_{g2}-orbitals [63]. This changes the orbital symmetry of the e_g electrons at the Mn^{3+} sites inducing the destabilization and relaxation of the JT distortions of the surrounding MnO_6 octahedra, generating high energy lattice vibrations as schematically depicted in figure 28 [60, 64, 65]. This is actually confirmed in the recent experiment by Beaud *et al.* where the melting of the CO/OO phases and excitation of the optical phonon modes are observed under optical stimulus [60]. Hence, the high energy vibrations *i.e.* phonon modes are induced in the lattice due to the illumination. These lattice vibrations and already destabilized CO/OO phase lead to the greatly reduced magnetic field for the IMT as the already vibrating spins are easier to flip along the background magnetic field [**P5**]. This also explains why an increase of temperature reduces the insulator-to-metal and metamagnetic AFM to FM transition fields as the low energy phonons/vibrations are created into the lattice due to heating effect. However, the optical stimulus alone cannot turn the sample into the

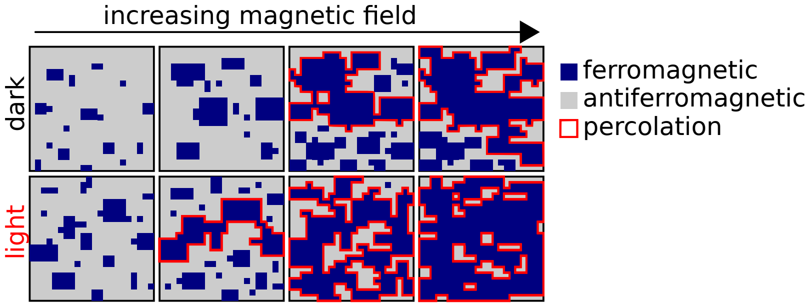

Figure 29. A schematic illustration of the nanoscale phase separation in manganites and the influence of optical stimulus to the AFM insulator and FM metallic cluster dynamics under the increasing magnetic field. The IMT occurs in a certain magnetic field during the metamagnetic AFM to FM phase transition when the FM metallic clusters form a solid percolation path through the sample. The illumination increases the efficiency of the magnetic field increasing the FM metallic clusters in the sample and hence the IMT transition occurs at the reduced magnetic field. [**P5**]

metallic phase as the magnetic field is needed to flip the spins to achieve the FM phase. Hence, the CMR and metamagnetic transition effects are only visible below T_N: the formation of the AFM phase activates the spin degree of freedom of the system which can be influenced with the magnetic field [**P5**].

The effects of illumination are the most prominent below 50 K where the films have a frustrated magnetic phase with high thermomagnetic irreversibility. Initially, in this frustrated magnetic phase, with a nanoscale phase separation between AFM and FM clusters, the AFM phase dominates [26], as shown in figure 29. The increase of the background magnetic field makes the FM phase energetically more favourable and rises the FM/AFM cluster ratio in the samples. The illumination gives the frustrated spins an extra push to overcome the free energy barrier to obtain the prevailing energy minimum. Hence, the illumination enhances the content of the FM clusters in the presence of the magnetic field in the PCMO samples [66]. This reduces the IMT field, as in the metallic phase, the FM metallic clusters establish a solid conducting path through the sample, as schematically illustrated in figure 29. When the system is in metallic state and magnetic field is turned off, this process works another way around, as illumination drives the system towards more insulating state (figure 26(c)).

This percolative conducting process also explains the much sharper drop in the resistivity curve when compared with the metamagnetic AFM to FM transition seen in the magnetization curve. The magnetic signal comes from the whole sample, whereas already few conducting paths through the sample give rise to the metallic response in resistivity measurements [**P5**]. Also, after the IMT transition, the resistivity continues to slowly decrease with the increasing magnetic field, indicating the formation of even more FM metallic clusters (figure 23).

6 Conclusions

In this thesis, a series of polycrystalline PCMO samples with varying calcium concentration $x =$ 0.0 - 0.5 were successfully synthesized with solid state reaction method. The structural characterization of the polycrystalline samples at room temperature showed a reduction of the unit cell volume and improvement in perovskite structure symmetry. With increasing Ca concentration the distortion in the perovskite structure was reduced.

By controlling the Ca concentration, substantial differences in the magnetic properties of the polycrystalline samples were achieved as the modified Mn^{3+}/Mn^{4+} ion ratio in the samples affected the prevailing magnetic interactions. The ac and dc magnetic characterizations of the samples showed versatile magnetic properties having signatures of coexisting AFM-FM ordering with cluster glass behaviour arising from the magnetic frustration between the competing AFM and FM clusters. In the low doping regime between $x =$ 0.0 - 0.2, increasing the hole doping induced an evolution of the FM phase while the AFM phase was diminished. However, further increase of the Ca concentration, from $x =$ 0.3 to 0.5, quickly reduced the FM phase in the samples as the Mn^{3+}/Mn^{4+} ratio decreased closer to 1, increasing also the AFM CO/OO phase that is most effective in the sample $x =$ 0.5.

The AFM CO/OO phase could be melted with high external magnetic field at temperatures below T_{N}, inducing an irreversible first order metamagnetic AFM to FM phase transition. The strength of the AFM CO/OO phase and the magnetic melting field value decreased with decreasing Ca concentration and increasing temperature. Additionally, in the polycrystalline samples the reverse transition from the metastable FM to the AFM phase was only achieved by increasing the temperature to overcome the strong pinning potential of this material.

The PCMO thin films grown from the polycrystalline target samples with $x =$ 0.4 and 0.5 showed a great reduction in the magnetic field required to melt the AFM CO/OO phase when compared to polycrystalline samples. The strength of the AFM CO phase could be further decreased in thin films by using low *in situ* oxygen annealing temperature of 500 °C after deposition. As shown in the the magneto-transport measurements of the thin films, the melting of AFM CO/OO phase was connected to CMR effect where the magnetic field induced IMT. A better crystalline quality and increased Mn^{3+}/Mn^{4+} ratio due to the low temperature ablation process was concluded to be the reason for the decreased IMT field in the thin film samples annealed at $T_{\text{a}} =$ 500 °C.

The colossal magnetoresistive insulator to metal switching under the significantly reduced magnetic field was achieved by illuminating the PCMO thin film samples. The thin films' resistive response to dynamic illumination was different depending on the prevailing magnetic phase of the films as well as on the external magnetic field value. Furthermore, by magnetically biasing the thin films with constant external magnetic field, the IMT could be tuned to be extra sensitive to the illumination. In addition, the intensity of the IMT could be further fine tuned by varying the laser fluence and the exposure time. However, the IMT did not occur solely under illumination but the magnetic field was observed to be necessary to complete the transition. The illumination effects were concluded to originate from the light induced relaxation of JT distortion. This excites the optical phonon modes weakening the AFM CO/OO phase, leading to the reduction of the IMT field.

This kind of cooperative influence of multiple external stimuli, which together enhances the efficiency of the phase transition, can be very useful in future applications of manganites.

References

[1] V.M Goldschmidt, Naturwissenschaften **14**, 477 (1926).

[2] J. P. Zhou *et al.*, Appl. Phys. Lett. **75**, 1146 (1999).

[3] J. Crangle, *Solid State Magnetism* (Edward Arnold publishers, 1991).

[4] J. M. D. Coey, *Magnetism and magnetic materials* (Cambridge University Press, 2010).

[5] Y. Tokura, *Colossal magnetoresistive oxides* (Gordon and Breach Science, New York, 2000).

[6] H. A. Jahn and E. Teller, Proc. R. Soc. A **161**, 220 (1937).

[7] J.B Goodenough and L. Loeb, Phys. Rev. **98**, 391 (1955).

[8] J. B. Goodenough, Physical Review **100**, 564 (1955).

[9] J. Kanamori, J. Phys. Chem. Solids **10**, 87 (1959).

[10] P.W. Anderson, Phys. Rev. **115**, 2 (1959).

[11] C. Zener, Physical Review **81**, 440 (1951).

[12] P. W. Anderson and H. Hasegawa, Physical Review **100**, 675 (1955).

[13] A. J. Millis, P. B. Littlewood, and B. I. Shraiman, Phys. Rev. Lett. **74**, 5144 (1995).

[14] T. V. Ramakrishnan, H. R. Krishnamurthy, S. R. Hassan, and G. Venketeswara Pai, Phys. Rev. Lett. **92**, 157203 (2004).

[15] C. Kittel, *Introduction to Solid State Physics, 8th ed.* (John Wiley & Sons, Inc, 2005).

[16] F. Duan and J. Guojun, *Introduction to Condensed Matter Physics, Volume 1* (World Scientific Publishing, 2005).

[17] G. H. Jonker and J. H. van Santen, Physica **16**, 337 (1950).

[18] M. Imada, A. Fujimori, and Y. Tokura, Rev. Mod. Phys. **70**, 1039 (1998).

[19] A. Abrikosov, *Fundamentals of The Theory of Metals* (North-Holland, 1988).

[20] A. J. Millis, Boris I. Shraiman, and R. Mueller, Phys. Rev. Lett. **77**, 175 (1996).

[21] Y. Tokura and Y. Tomioka, J. Magn. and Magn. Mater. **200**, 1 (1999).

[22] A. Martinelli *et al.*, Phys. Rev. B **73**, 064423 (2006).

[23] M. R. Lees, J. Barratt, G. Balakrishnan, and D. McK. Paul, Phys. Rev. B **58**, 8694 (1997).

[24] K. J. Thomas *et al.*, Phys. Rev. Lett. **92**, 237204 (2004).

[25] V. B. Shenoy and C. N. R. Rao, Phil. Trans. R. Soc. A **366**, 63 (2008).

[26] A. Dagotto, T. Hotta, and A. Moreo, Physics Reports **344**, 1 (2001).

[27] E. Dagotto, *Nanoscale Phase Separation and Colossal Magnetoresistance: The Physics of Manganites and Related Compounds* (Springer-Verlag, Berlin, 2003).

[28] Y. Imry and M. Wortis, Phys. Rev. B **19**, 3580 (1979).

[29] R. C. Ropp, *Solid State Chemistry* (Elsevier Science B.V, 2003).

[30] D. B. Chrisey and G. K. Hubler, *Pulsed Laser Deposition of Thin Films* (John Wiley Sons Inc., 1994).

[31] A. W. Bailey and A. Modak, J. Thermophys. **3**, 42 (1989).

[32] D. J. Krajnovich, J. E. Vazquez, and R. J. Savoy, Science **259**, 1590 (1993).

[33] J. Als-Nielsen and D. McMorrow, *Elements of modern x-ray physics* (Wiley, 2010).

[34] J. Rodriguez-Carvajal, Abstracts of the Satellite Meeting on Powder Diffraction of the XV Congress of the IUCr 127 (1990).

[35] K. H. J. Buschow and F. R. Boer, *Physics of Magnetism and Magnetic Materials* (Kluwer Academic Publishers, 2003).

[36] Ch. Jooss *et al.*, Proc. Natl. Acad. Sci. U.S.A. **104**, 13597 (2007).

[37] Z. Jirak *et al.*, J. Magn. and Magn. Mater. **53**, 153 (1985).

[38] Z. Jirak, S. Vratislav, and J. Zajicek, Phys. Stat. Sol. A **52**, K39 (1979).

[39] Huali Yang *et al.*, Phys. Rev. B **91**, 174405 (2015).

[40] X. H. Huang *et al.*, J. Appl. Phys. **106**, 083904 (2009).

[41] S. Mukherjee, R. Ranganathan, P. S. Anilkumar, and P. A. Joy, Phys. Rev. B **54**, 9267 (1996).

[42] X. G. Li *et al.*, J. Appl. Phys. **85**, 1663 (1999).

[43] J. Tikkanen *et al.*, J. Phys. Cond. Mat. **28**, 036001 (2016).

[44] J. A. Mydosh, *Spin Glasses: An Experimental Introduction* (Taylor and Francis, London, 1993).

[45] S. Kundu and T. K. Nath, J. Magn. and Magn. Mater. **322**, 2408 (2010).

[46] J. R. L. de Almeida and D. J. Thouless, J. Phys. A **11**, 983 (1978).

[47] T. Zhang, T. F. Zhou, T. Qian, and X. G. Li, Phys. Rev. B **76**, 174415 (2007).

[48] G. G. Kenning, D. Chu, and R. Orbach, Phys. Rev. Lett. **66**, 2923 (1991).

[49] R. V. Chamberlin, M. Hardiman, L. A. Turkevich, and R. Orbach, Phys. Rev. B **11**, 6720 (1982).

[50] D. Petit, L. Fruchter, and I. A. Campbell, Phys. Rev. Lett. **83**, 5130 (1999).

[51] S. D. Tiwari and K. P. Rajeev, Phys. Rev. B **72**, 104433 (2005).

[52] F. H. Aragón *et al.*, Physica B **407**, 2601 (2012).

[53] K. R. Mavani and P. L. Paulose, Eur. Phys. Lett. **78**, 37004 (2007).

[54] S. S. Rao and S. V. Bhat, J. Phys. Cond. Mat. **22**, 116004 (2010).

[55] H. Kuwahara *et al.*, Science **270**, 961 (1995).

[56] Anamitra Mukherjee *et al.*, Phys. Rev. Lett. **110**, 157201 (2013).

[57] M. J. Calderón, A. J. Millis, and K. H. Ahn, Phys. Rev. B **68**, 100401(R) (2003).

[58] Z. Q. Yang *et al.*, Appl. Phys. Lett. **88**, 072507 (2006).

[59] W. Prellier *et al.*, Phys. Rev. B **62**, R16337 (2000).

[60] P. Beaud *et al.*, Nature Materials **13**, 923 (2014).

[61] S. M. Sze, *Semiconductor devices Physics and Technology* (John Wiley & Sons, 1985).

[62] H. Wadati *et al.*, New J. Phys. **16**, 033006 (2014).

[63] J. H. Jung *et al.*, Phys. Rev. B **57**, R11043 (1997).

[64] P. Beaud *et al.*, Phys. Rev. Lett. **103**, 155702 (2009).

[65] P. Polli *et al.*, Nature Mater. **6**, 643 (2007).

[66] S. Majumdar *et al.*, J. Phys. Cond. Mat. **23**, 466002 (2011).